The Astrophysical Journal, 914:61 (17pp), 2021 June 10 https://doi.org/10.3847/1538-4357/abe40b

Discovery of Beryllium in White Dwarfs Polluted by Planetesimal Accretion

Beth L. Klein[1], Alexandra E. Doyle[2], B. Zuckerman[1], P. Dufour[3,4], Simon Blouin[5], Carl Melis[6], Alycia J. Weinberger[7], and Edward D. Young[2]
[1] Department of Physics and Astronomy, University of California, Los Angeles, CA 90095-1562, USA; kleinb@astro.ucla.edu
[2] Earth, Planetary, and Space Sciences, University of California, Los Angeles, Los Angeles, CA 90095, USA
[3] Institut de Recherche sur les Exoplanètes (iREx), Université de Montréal, Montréal, QC H3C 3J7, Canada
[4] Département de physique, Université de Montréal, Montréal, QC H3C 3J7, Canada
[5] Los Alamos National Laboratory, P.O. Box 1663, Mail Stop P365, Los Alamos, NM 87545, USA
[6] Center for Astrophysics and Space Sciences, University of California, San Diego, CA 92093-0424, USA
[7] Earth and Planets Laboratory, Carnegie Institution for Science, 5241 Broad Branch Road NW, Washington, DC 20015, USA
Received 2020 December 9; revised 2021 February 2; accepted 2021 February 5; published 2021 June 15

Abstract

The element beryllium is detected for the first time in white dwarf stars. This discovery in the spectra of two helium-atmosphere white dwarfs was made possible only because of the remarkable overabundance of Be relative to all other elements, heavier than He, observed in these stars. The measured Be abundances, relative to chondritic, are by far the largest ever seen in any astronomical object. We anticipate that the Be in these accreted planetary bodies was produced by spallation of one or more of O, C, and N in a region of high fluence of particles of MeV or greater energy.

Unified Astronomy Thesaurus concepts: White dwarf stars (1799); Abundance ratios (11); Overabundances (1192); High resolution spectroscopy (2096); Stellar spectral lines (1630); Stellar accretion (1578); Planetesimals (1259); Extrasolar rocky planets (511)

1. Introduction

Over the past decade or so, the presence of absorption lines from elements heavier than helium in the spectra of single white dwarfs (WDs) with $T_{\rm eff} \lesssim 25{,}000$ K, has come to be understood without a doubt as the result of accretion of disrupted planet(esimal)s from their ancient planetary systems (e.g., reviews by Jura & Young 2014; Veras 2016; Farihi 2016; Zuckerman & Young 2018).[8] As a result, our knowledge and understanding of the compositions of exoplanets have grown significantly through the extraordinary detail and precision afforded by this powerful observational technique. To date, exoplanetesimal compositions measured in WD atmospheres that are "polluted" with accreted material are mostly similar to rocky bodies in the solar system, with some interesting exceptions that include water-rich bodies (Farihi et al. 2011, 2013; Raddi et al. 2015; Xu et al. 2017; Gentile Fusillo et al. 2017; Hoskin et al. 2020). Although nothing as bizarre as a carbon-dominated planet (e.g., Bond et al. 2010) has ever been revealed in studies of WDs, significant variations in overall element-to-element abundance ratios have been measured among various WDs. Such variations are generally attributed to sampling of material affected by igneous differentiation, i.e., originating primarily from the crust and mantle (Zuckerman et al. 2011; Melis & Dufour 2017) or core (Melis et al. 2011; Gänsicke et al. 2012) portions of a differentiated rocky body.

However, what has previously not been seen is a dramatic deviation of the abundance of a specific element from an (understandable) overall pattern of elements. In the present paper, we report the discovery of beryllium (Be) with remarkably high abundances relative to those of the elements magnesium, silicon, and iron in two WDs: GALEX 2667197548689621056 (23:39:17.03, −04:24:24.7, J2000; hereafter GALEXJ2339) and GD 378 (18:23:37.01, +41:04:02.1, J2000). In both stars the Be is overabundant by about two orders of magnitude. This is, far and away, the largest abundance of Be relative to chondritic ever measured in any astronomical object.

Since the earliest observations of WDs a century ago, a growing list of accreted elements has been fundamental in understanding WD pollution and associated cosmochemical insights. Similar to many fields in astronomy, the progress over time for new detections generally traces the capabilities enabled by the available observational facilities, as well as the commitment by observers to consider the best targets. Table 1 is an attempt to summarize the progress of new element identifications in WD atmospheres polluted by accreted planetary material.

The first identifications of the WD pollution were found in optical spectra through the Ca II H and K resonance lines in cool helium-atmosphere WDs[9] beginning with the iconic vMa2 (van Maanen 1917). While van Maanen was looking for companions to high-proper-motion stars, he unwittingly observed a polluted white dwarf. It took much longer (almost a century!) until it was appreciated that van Maanen's observation was in fact the first evidence of the existence of an extrasolar planetary system (Zuckerman 2015; Farihi 2016).

Mg and Fe were next to be identified in optical spectra (Kuiper 1941; Greenstein 1956), followed later by Na (Greenstein 1976). Then the International Ultraviolet Explorer (IUE) satellite opened up access to ultraviolet (UV) wavelengths where elements such as Si could be detected (Cottrell & Greenstein 1980). Also, since Mg and Fe are more readily detected in this spectral region, the IUE significantly increased the number of known polluted WDs of the time (review by Koester 1987). Meanwhile, the minor element Cr was identified in optical spectra by Wehrse & Liebert (1980).

[8] With the exception of the subset of WDs where carbon has been dredged-up from the interior (Koester et al. 1982).

[9] Ca equivalent widths in these stars can be $\gtrsim$40 Å (e.g., Liebert et al. 1987).

Table 1
History of Element Discovery from Accreted Planetary Material in White Dwarfs Cooler Than 25,000 K

Discovery Year	Polluting Element(s)	WD	Facility	Reference	Notes
1917	Ca	vMa2	Mount Wilson	vM1917	First ever exoplanet evidence
1941	Mg?	Ross 640	McDonald	K1941	"probably Mg"
1956	Fe	vMa2	Hale	G1956	Blended Fe I
1960	Mg	vMa2	Hale	W1960	Figure 6 in W1960
1976	Na	G165-7	Hale	G1976	Figure 1 in G1976
1980	Si	Ross 640	IUE	CG1980	
1980	Cr	G165-7	Lick/IDS	WL1980	
1991	C?	G238-44	IUE	V1991	Section 2.1 in H1997
1995	C, O?, Al?	GD 40	HST/FOS	S1995	O and Al unclear
1998	Al	G238-44	IUE	H1998	
2007	Sc, Ti, V, Mn, Co, Ni, Cu, Sr	GD 362	Keck/HIRES	Z2007	Earth/Moon-like composition
2008	O, S	GD 378, GD 61	FUSE	D2008	Unambiguous O
2012	P	GD 40, G241-6, GALEXJ1931	HST/COS	J2012, G2012	
2017	N	G200-39	HST/COS	X2017	Extrasolar KBO
2021	Li, K	WDJ1644 (+others w/Li)	SOAR/Goodman	K2021	
2021	Li, K	LHS 2534 (+others w/Li)	VLT/X-shooter	H2021	
2021	Be	GALEXJ2339, GD 378	Keck/HIRES	This paper	Spallation

Note. We trace the discovery of elements that unambiguously come from accretion of planetary material. To that end we restrict this discovery timeline to WDs cooler than 25,000 K so as to avoid confusion with other processes such as radiative levitation (see discussion in the text). The discovery year is associated with the paper in which unambiguous spectral features associated with a given element were first identified. In many cases an abundance analysis came later. The comment "(+ others w/Li)" in the two "Li, K" rows indicates that there are additional WDs in those studies in which Li (but not K) were detected. References are: vM1917 (van Maanen 1917); K1941 (Kuiper 1941); G1956 (Greenstein 1956); W1960 (Weidemann 1960); G1976 (Greenstein 1976); CG1980 (Cottrell & Greenstein 1980); WL1980 (Wehrse & Liebert 1980); V1991 (Vennes et al. 1991); S1995 (Shipman et al. 1995); H1997 (Holberg et al. 1997); H1998 (Holberg et al. 1998); Z2007 (Zuckerman et al. 2007); D2008 (Desharnais et al. 2008); J2012 (Jura et al. 2012); G2012 (Gänsicke et al. 2012); X2017 (Xu et al. 2017); K2021 (Kaiser et al. 2021); and H2021 (Hollands et al. 2021).

As early as 1981, many of the major and minor elements, such as: C, N, O, Al, Si, P, S, Mn, and Ni were found in UV spectra of very hot WDs (effective temperature $T_{\rm eff} \gtrsim$ 60,000 K; Bruhweiler & Kondo 1981; Dupree & Raymond 1982; Sion et al. 1985; Holberg et al. 1993, 1994; Vennes et al. 1996). However, since radiative levitation can have an important effect at effective temperatures higher than 25,000 K (Koester et al. 2014 and references therein), the origin of heavy elements in such stars is unclear. We are aware of analyses that argue that heavy elements in some hot WDs are accreted (e.g., Vennes et al. 1996; Barstow et al. 2014; Wilson et al. 2019a; Schreiber et al. 2019), although from which source(s) remains uncertain.

Referring to WDs cooler than 25,000 K, carbon was observed in IUE spectra of some WDs with $T_{\rm eff} < 13{,}000$ K (e.g., Wegner 1981), but those turned out to be due to dredge-up (Koester et al. 1982), not planetesimal accretion. As far as we know, in WDs cooler than 25,000 K, carbon accreted from planetary material was first unambiguously identified in GD 40 via Hubble Space Telescope (HST) Faint Object Spectrograph (FOS) observations by Shipman et al. (1995). Shipman et al. (1995) also reported possible, but uncertain/blended, detections of O and Al. Al was clearly detected in G238-44, by IUE, as reported in the survey by Holberg et al. (1998), while the Far Ultraviolet Spectroscopic Explorer (FUSE) satellite brought the unambiguous identifications of O and S in GD 378 and O in GD 61 (Desharnais et al. 2008).[10]

A dramatic breakthrough occurred when the High Resolution Echelle Spectrograph (HIRES; Vogt et al. 1994) on the Keck I Telescope was used to observe the extremely polluted WD, GD 362. Those spectra displayed absorption lines of 15 elements heavier than He (Zuckerman et al. 2007) including the trace elements Sc and Sr with abundances nine orders of magnitude less than H. The pattern of element abundances in this WD led to the conclusion that it had accreted a planetary body with a composition similar to a rocky planetesimal. HST/COS added P in GD 40, G241-6, and GALEXJ1931 + 0117 (Jura et al. 2012; Gänsicke et al. 2012), and N in G200-39 (=WD1425+540, Xu et al. 2017), where in the latter case, the polluting parent body is an extrasolar Kuiper Belt analog. Note that G200-39 has a common proper-motion main-sequence companion, G200-40, and sometimes their names have been confused in the literature.

Recently, with parallax and photometry measurements from Gaia DR2 (Gaia Collaboration et al. 2016, 2018), it has been possible to identify previously unknown WDs from photometric colors and absolute magnitudes. Thanks to those data, studies covering the cooler end of the WD sequence have recently resulted in the detections of Li and K, by two independent groups (Kaiser et al. 2021; Hollands et al. 2021). In this paper, using Gaia DR2 along with the exquisite sensitivity of Keck/HIRES at wavelengths as short as 3130 Å, we have the first detection of Be in the atmospheres of two polluted WDs: GALEXJ2339 and GD 378 (Figures 1 and 2).

GD 378 has been known for a long time to be a WD with a helium-line dominated spectrum (spectral type[11] DB), identified half a century ago by Greenstein (1969) and later found to

[10] In re-examination, lines of P are also present in the FUSE spectrum of GD 378, but were not identified by Desharnais et al. (2008).

[11] Spectral classifications in this paper follow the system of Sion et al. (1983): the first letter in a white dwarf type is D (degenerate star), followed by letters representing the optically detected presence of spectral features from: hydrogen (A), helium (B), and elements heavier than H or He (Z) in decreasing order of the observed line strengths.

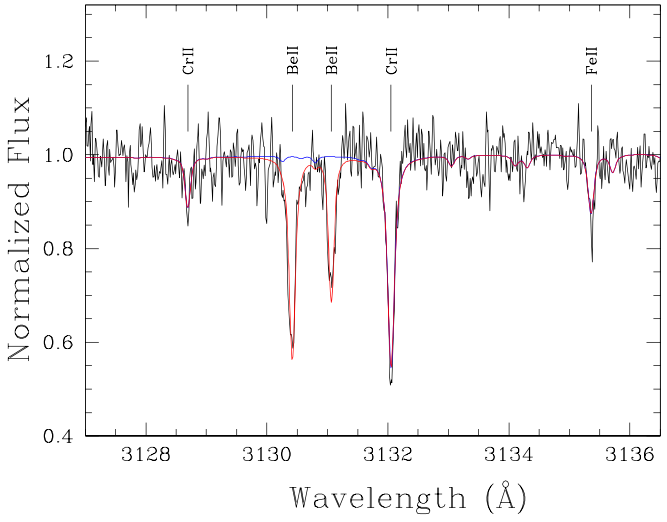

Figure 1. Be II detection in GALEXJ2339 from Keck/HIRES. Wavelengths are in air and the laboratory rest frame. The data are plotted in black, and the red line is our best-fit model. The blue line is the same model, but with the abundance of Be set to zero, demonstrating that the absorption features at 3130.42 and 3131.06 Å come from Be, without significant contribution from other elements.

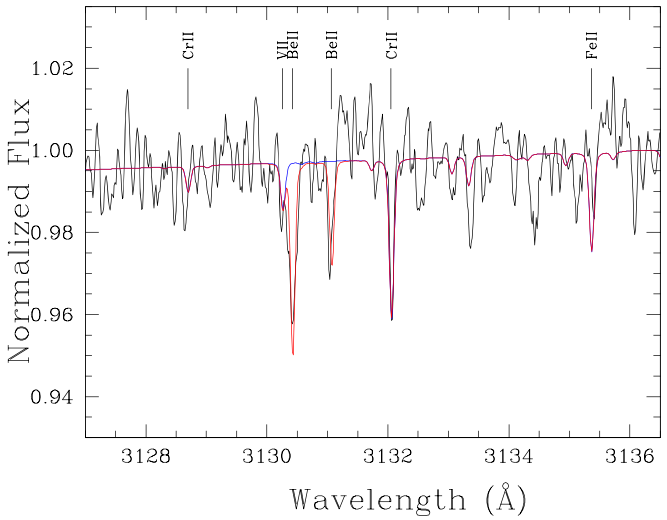

Figure 2. Be II detection in GD 378, similar to Figure 1, but smoothed by a five-point boxcar average for clarity. A possible small contribution from V II 3130.26 Å to the blue wing of the Be II 3130.42 Å line is shown in our model, but this is only based on a measured upper limit for V.

also display hydrogen lines (DBA) Greenstein (1984). The detection of calcium absorption in GD 378 elevated it to the category of being one of the first of three known DBAZ stars, including GD 61 and G200-39 (Sion et al. 1988; Kenyon et al. 1988).

In contrast to the well-known GD 378, the newly found GALEXJ2339 was only recently identified as a WD (coincidentally in time, by the spectroscopic efforts described in this paper and the 100 pc sample of Kilic et al. 2020), thanks to Gaia DR2 and the subsequent assembly of WD-candidate catalogs (e.g., Gentile Fusillo et al. 2019; Jiménez-Esteban et al. 2018). Low-resolution optical spectroscopy of GALEXJ2339 reveals the presence of H, He, and elements of higher Z. Since the H lines are the strongest optical features, followed by the He lines, and then the Ca II K-line, we classify this star as spectral type DABZ. Nonetheless, our atmospheric models show that the composition is predominantly helium. Thus GALEXJ2339 is another example of a heavily polluted WD with a helium-dominated atmosphere, but whose spectral type starts with "DA," as the Balmer hydrogen lines are the strongest features in its optical spectrum,[12] with equivalent widths (EWs) greater than those of either the He or heavy element (Ca II H and K) lines (e.g., Koester et al. 2005; Zuckerman et al. 2007; Raddi et al. 2015).

High-resolution optical spectroscopy of GALEXJ2339 reveals absorption lines of many elements, with the surprising appearance of two relatively strong lines from beryllium (Figure 1), *an element that has not been seen before in a WD of any type*.

The visibility of the Be lines in GALEXJ2339 reminded us of a previously noted hint of a line in our 2008 HIRES spectrum of GD 378, near the wavelength of the strongest Be line. This led to a follow-up HIRES observation, which improved the signal-to-noise ratio (S/N) enough to detect both Be lines in GD 378 (Figure 2). We also re-examined data sets of other heavily polluted WDs to check for any similar features that may have been overlooked, but we found no other obvious detections of Be. Our abundance analyses for GALEXJ2339 and GD 378 described here show the measured Be ratios relative to other elements to be extraordinary in both stars, approximately two orders of magnitude higher than those measured in main-sequence stars and in meteorites.

This paper is organized as follows. In Section 2 we list our observations that led to this discovery, and in Section 3 we discuss the measurements of the absorption lines in both stars. Our atmosphere models are described in Section 4 along with plots of the detections of all elements in the spectra. Section 5 provides an analysis of the calculated abundances. Findings and conclusions are discussed in Section 6, but we also refer readers to this paper's companion paper by Doyle et al. (2021) for an extensive interpretation of our findings. Some topics regarding model fitting and uncertainty calculations are detailed in Appendices A and B.

2. Observations

2.1. GALEXJ2339

2.1.1. KAST

We first observed GALEXJ2339 on 2018 December 28 (UT) with the KAST Spectrograph[13] on the 3 m Shane telescope at Lick Observatory as part of our large-scale survey to search for heavily polluted WDs among newly identified WD candidates from Gaia DR2 (Gentile Fusillo et al. 2019; Melis et al. 2018). Our setup employed a 2″ slit with the d57 dichroic splitting light to the blue arm 600/4310 grism and red arm 830/8460 grating, providing coverage of 3450–7800 Å and a resolving power $R = \frac{\lambda}{\Delta\lambda} \simeq 700$ in the blue and ≃2300 in the red.

The data were reduced using standard IRAF (Tody 1986) slit spectra routines. The resulting spectrum has an S/N per pixel of ≃35 near 4500 Å and ≃26 near 7500 Å. Absorption lines

[12] There appears to be some confusion in the literature recently in which classical DZ stars such as Ross 640, L745-46A, and PG1225−079 have been referred to as DA white dwarfs and/or categorized as having the Balmer lines "dominate" their spectral classification. Our observation is that these particular WDs are not dominated optically by hydrogen lines since the Ca II H and K lines are the strongest features in the optical spectra. Following the WD classification system of Sion et al. (1983), they are DZA(B).

[13] https://mthamilton.ucolick.org/techdocs/instruments/kast/

from both H I and He I are clearly detected, and the Ca II K-line and Mg II 4481 Å are apparent in these data.

A second KAST spectrum was obtained on 2019 July 12, with a shifted red arm setup that covers the Ca infrared triplet (λ8498/8542/8662 Å) to check if GALEXJ2339 might be another addition to the small, but growing, set of gas disk emission systems (Melis et al. 2020; Dennihy et al. 2020; Gentile Fusillo et al. 2020). A 1.″5 slit was used with a similar instrument setup as described above, except with the 830/8460 grating position shifted toward the red. The resulting red arm spectrum covers 6440−8750 Å at a resolving power of ≃2300 with an S/N ≃42 near 7500 Å. In addition to the various H I and He I lines, the O I 7772 Å triplet (unresolved), as well as a weak O I 8446 Å feature, were detected in this spectrum. No emission was detected from the Ca II infrared triplet or any other parts of GALEXJ2339's spectrum.

2.1.2. MagE

A moderate-resolution optical spectrum of GALEXJ2339 was acquired with the MagE echellette spectrograph on the Magellan 1 (Baade) telescope at Las Campanas Observatory on 2019 July 3. The target was observed for 3000 s through the 0.″5 slit, for a resolving power of $R \simeq 8000$. Data reduction including flat-fielding, spectral extraction, and wavelength calibration was performed with the Carnegie Python pipeline (Kelson et al. 2000; Kelson 2003). All in one shot, these MagE data covered wavelengths from 3110 to 10000 Å with an S/N of ≃10 at 3130 Å (near the Be lines), ≃50 at 4485 Å, ≃65 near 5170 Å, ≃30 near 7770 Å, and ≃25 near 8500 Å. This spectrum confirmed the detection of O I 7772, the nondetection of gas-emission features from the Ca II infrared triplet, and discovered absorption lines from the Mg I 3838 triplet, Mg I 5184, Ca II 3706/3737, Si II 3856/3863, Si II 6347/6371, Ca II 8542/8662, and a hint of Mg II 7896.

2.1.3. HIRES

On 2019 July 7 (UT), we used HIRES (Vogt et al. 1994) on the Keck I Telescope at Maunakea Observatory, configured with the blue collimator to observe GALEXJ2339. The C5 decker (slit width 1.″148) provided a resolving power of $R \simeq 40{,}000$ and wavelength coverage of 3120–5950 Å. Data were reduced with similar methods and routines as described in Klein et al. (2010), using both IRAF and the MAKEE[14] software reduction packages. In excellent conditions (clear skies, 0.″6 seeing), a 3000 s integration resulted in a spectrum with S/N ≃23 around 3130 Å near the Be lines, ≃50 near 4481 Å, and ≃35 near 5170 Å. On 2020 October 7, we obtained two hours of integration with the HIRES red collimator and C5 decker (again with clear skies, 0.″6 seeing), resulting in a spectrum of wavelengths from 4750 to 9000 Å with S/N ≃80 near 5170 Å, ≃45 near 7770 Å, and ≃40 near 8500 Å.

2.2. GD 378

2.2.1. HIRES

GD 378 was observed with the HIRES blue collimator for 3900 s on 2008 February 13 (UT) and red collimator for 2400 s on 2008 February 26 (UT). Observing conditions were good with 0.″7 seeing on 2008 February 13 and 0.″8 on 2008 February 26. The instrument setups and data reduction were similar to those described above, although for GD 378's red data, an additional re-normalizing processing step was applied to calibrate and remove second-order flux contamination in the region 8200–9000 Å as described in Klein et al. (2010) and Melis et al. (2010).

Recently, on 2020 October 8, with clear skies and 0.″6 seeing, we obtained an additional 4000 s integration with the HIRES blue collimator. This resulted in an S/N of 90 near 3130 Å and ≃150 near 5170 Å in the final co-added blue spectra. The S/N of the red spectrum is ≃85 near 5170 Å, ≃50 near 7770 Å, and ≃32 near 8500 Å.

2.2.2. FUSE

Far-UV observations of GD 378 were made with the FUSE satellite on 2004 May 22 (UT) under program ID D168 (PI: F. Wesemael). The wavelength range is 905–1185 Å with $R \simeq 15{,}000$. These UV data provide coverage of elements (especially volatiles) that are generally not accessible from ground-based optical facilities, so we decided to re-analyze the FUSE spectrum with our updated model codes and abundance fits in coordination with our HIRES data. We downloaded the spectra from the Mikulski Archive for Space Telescopes (MAST), which were processed using the CALFUSE pipeline version 3.2. Desharnais et al. (2008) previously published an abundance analysis of the FUSE data including identifications of C, O, Si, S, and Fe. In the present paper, we confirm the identifications of these elements, and we also identify phosphorous in the photosphere of GD 378.

3. Spectral Measurements

3.1. Absorption Lines

Through all of these observations, spectra rich with absorption lines appear in both stars. Line lists are given in the Appendix (Tables 7 and 8), including the detections of the Be II resonance doublet at 3130.42 and 3131.06 Å, shown in Figures 1 and 2. These are the only observable optical beryllium lines—the same ones used to obtain Be abundances in main-sequence stars (Boesgaard 1976a), giant stars (Boesgaard et al. 2020), and the Sun (Chmielewski et al. 1975). Unlike main-sequence stars, the Be lines in these WD spectra are almost entirely free from blending with lines of other elements, so we can be confident that our measured line strengths and derived abundances are not confused. The Be doublet lines arise out of the ground state, but to date, no detection from the interstellar medium (ISM) has been made with a strict upper limit of $(^9\mathrm{Be/H}) \leqslant 7 \times 10^{-13}$ (Hebrard et al. 1997). Given these prior ISM studies, and that our measured radial velocities (RVs) are in excellent agreement with absorption lines of other elements (Figures 3 and 4), we conclude that the origin of the Be lines is photospheric in the two WDs.

3.2. Radial Velocities

RVs are calculated from Doppler shifts of the measured line centers relative to laboratory wavelengths. Figures 3 and 4 show histograms of measured RVs for the sets of absorption lines for each star. The plotted velocities, relative to the Sun, are not adjusted for the gravitational redshifts of the WDs, so

[14] https://www.astro.caltech.edu/~tb/makee/

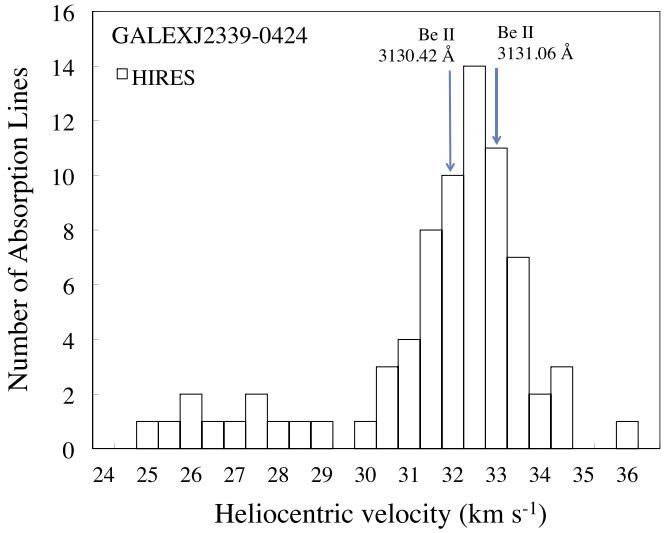

Figure 3. Heliocentric RVs of absorption lines from Table 7. The Be lines have velocities consistent with the other heavy element lines observed from the WD photosphere and thus are photospheric. The low-velocity tail between 25 and 28 km s^{-1} comes from the O I lines 7772/7774/7775/8447 Å, the Mg I triplet 5167/5173/5184 Å, and the doublet of Si II at 6347/6371 Å. See the text for additional comments on these somewhat shifted RV lines.

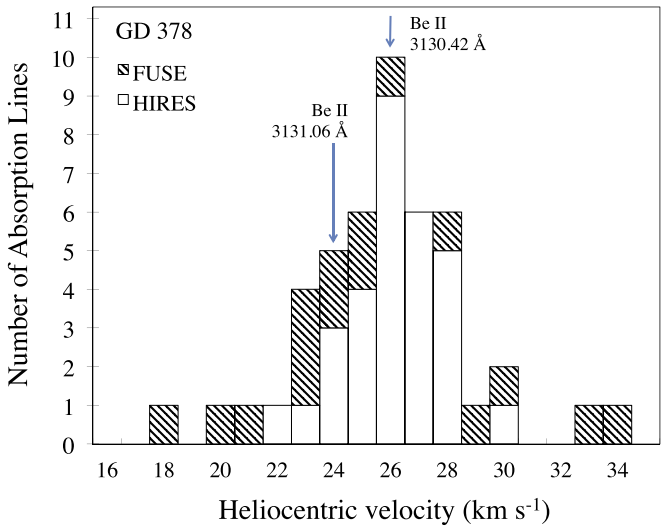

Figure 4. Heliocentric RVs of absorption lines from Table 8. Similar to GALEXJ2339, the Be lines in GD 378 are clearly photospheric. FUSE RVs are only from the spectral range $\lambda < 1100$ Å, as described in the text.

the RVs of the photospheric absorption lines represent the WD space motion (kinematic velocity) plus the gravitational redshift. The primary takeaway point from these plots is that, in both stars, the Be lines are consistent with coming from the WD photospheres, but some additional observations are noted as follows.

GALEXJ2339's RV distribution has a modestly blueshifted tail, composed of lines of O I, Mg I, and Si II, that must be photospheric due to the high values of the lower energy levels of the transitions. Such particular behavior of specific elements/species has been noted previously from HIRES spectra of the polluted WD PG 1225−079 (in that case from Fe I; Klein et al. 2011, Figure 14). Similar to the RV differential in GALEXJ2339, the blueshifted lines in PG 1225 −079 are also offset by about 6 km s^{-1} from the peak of the RV distribution of the other WD absorption lines. Klein et al.

Table 2
WD Parameters

Parameter	J2339−0424	GD 378
G (mag)	16.2	14.3
Distance (pc)	90	44
$T_{\rm eff}$ (K)	13735 (500)	15620 (500)
log g	7.93 (0.09)	7.93 (0.06)
$M_{\rm WD}$ ($M_\odot$)	0.548 (0.051)	0.551 (0.031)
$R_{\rm WD}$ ($R_\odot$)	0.0133 (0.0008)	0.0133 (0.0005)
Grav. redshift (km s^{-1})	26.2 (4.0)	26.4 (2.5)
Cooling age (Myr)	241 (6)	157 (3)
log ($M_{\rm CVZ}/M_{\rm WD}$)	−5.29 (0.30)	−5.77 (0.25)
$\dot{M}$ (g s^{-1})	1.7 x 10^9	1.8 x 10^8

Note. Gmag and distance (inverse parallax) are from Gaia DR2. $M_{\rm WD}$, $R_{\rm WD}$, gravitational redshift, cooling age, and $M_{\rm CVZ}$ (CVZ=convection zone) are from the Montreal White Dwarf Database (MWDD; Dufour et al. 2017; http://dev.montrealwhitedwarfdatabase.org/evolution.html). Uncertainties given in parentheses represent the range in values for each parameter considered at the upper and lower limits of the $T_{\rm eff}$/log g models (as described in Section 4). $\dot{M}$ is the mass flow rate (see Section 5).

(2011) referenced the possible effects of Stark shifts by Vennes et al. (2011), but further investigation into the nature of these observations is beyond the scope of this work.

From GALEXJ2339's main peak distribution (RVs > 28 km s^{-1}), the average is 32.3 km s^{-1} with a standard deviation of 1.5 km s^{-1}. Since the measured lines for this star come exclusively from HIRES, this standard deviation represents a reasonable uncertainty in measured RVs from HIRES data with the setup as described in Section 2.1.3. Based on measurements of RV calibration stars, we add an additional 1 km s^{-1} uncertainty in the absolute scale. Using the above average RV and uncertainties, along with the gravitational redshift given in Table 2, we find a heliocentric kinematic velocity for GALEXJ2339 of $+6 \pm 5$ km s^{-1}.

For GD 378, RVs from HIRES and FUSE data are compared. However, we do not use the RVs of the eight photospheric lines from the region $\lambda > 1100$ Å of the FUSE spectrum, as those are all systematically offset from the main distribution, most likely due to differing wavelength calibrations of different spectroscopic segments of FUSE. Otherwise, the average photospheric RVs from FUSE and HIRES separately are in very good agreement at 25.4 and 26.1 km s^{-1}, respectively. The standard deviation from HIRES-only data is 1.7 km s^{-1} (similar to GALEXJ2339, and representative of the typical relative measurement uncertainty from such HIRES data), while relative RV uncertainties from FUSE spectra are estimated to be ∼5–6 km s^{-1} (e.g., Moos et al. 2002; Barstow et al. 2010). Using the more precise and accurate HIRES-only measurements for the WD total heliocentric velocity, and the gravitational redshift from Table 2, the kinematic velocity of GD 378 is -0.3 ± 4 km s^{-1}.

3.3. Nonphotospheric Lines

In both stars, there are observed lines that arise from the ground state and have measured RVs that significantly disagree with the RVs of the photospheric lines. We consider if their origins may be interstellar or circumstellar.

The Na I D resonance doublet (λ5889.95/5895.92 Å) is observed in GALEXJ2339 at an RV of -7 ± 1.5 km s^{-1}, i.e., blueshifted by 39 km s^{-1} from the photospheric average of

$32.3 \pm 1.5\,\mathrm{km\,s^{-1}}$, and thus clearly incompatible with the WD photosphere. These lines also do not agree very well with the kinematic (circumstellar) velocity of $+6 \pm 5\,\mathrm{km\,s^{-1}}$ within 1σ–2σ uncertainties, but could be considered in agreement at the 3σ level. Absorption from the intervening ISM may be a more likely source in this case, as the possible similarity with a line-of-sight ISM cloud velocity[15] (Redfield & Linsky 2008) would support an ISM origin. Together these observations suggest that the Na I D lines in GALEXJ2339 are probably formed in the ISM, but we do not rule out the possibility of a circumstellar origin.

In GD 378, nonphotospheric components of C II 1036.34, Ca II K (λ3933.66 Å), and O I 1039.23 Å are well separated in RV from the photospheric components of these lines and can even be seen resolved in the spectra presented in Section 5. Along with Ca II H (λ3968.47 Å) and the N I triplet 1134.17/1134.42/1134.98 Å, all lines within this set are observed at RVs around $\sim -20\,\mathrm{km\,s^{-1}}$, which is neither consistent with the WD photosphere ($26 \pm 3\,\mathrm{km\,s^{-1}}$) nor its kinematic (circumstellar) velocity ($-0.3 \pm 4\,\mathrm{km\,s^{-1}}$); however, this does agree well with at least one known line-of-sight cloud velocity (Redfield & Linsky 2008). Thus the features are almost certainly interstellar.

4. Model Atmospheres

In He-atmosphere WDs with temperatures $\lesssim$20,000 K, the presence of hydrogen and other elements can have a non-negligible effect on the atmospheric structure due to the additional opacity from these pollutants (Dufour et al. 2007, 2010; Coutu et al. 2019). Taking this into account, here we use the same methods and codes as described in Dufour et al. (2007) and Blouin et al. (2018), briefly summarized as follows. We started by fitting Sloan Digital Sky Survey (SDSS; Alam et al. 2015) *ugriz* photometry[16] and Gaia parallax simultaneously with the Ca II H and K region and Hα from low-resolution spectra. For GALEXJ2339, we use the Kast spectrum described in Section 2.1.1, and for GD 378, we use the spectrum obtained by Bergeron et al. (2011), described therein. This provides a first estimate of the effective temperature ($T_{\rm eff}$), gravity (log g), hydrogen abundance [H/He] ($\equiv$log n(H)/n(He)), and overall heavy element presence through [Ca/He] ($\equiv$log n(Ca)/n(He)), where all other elements up to Sr are included, scaled to Ca in CI chondrite proportions (Lodders 2003). No de-reddening corrections were applied since it is not expected to be significant for stars within 100 pc.

Next we compute an atmospheric structure using the above parameters and from it, grids of synthetic spectra for each element, which we interpolate to fit the abundances. With those grids, we run a fit of the HIRES data to obtain a first estimation of the abundances of all detected elements. We then recalculate the structure using these estimated abundances and repeat the fitting as many times as necessary until a stable solution is found. From this procedure, we set our best-fit estimation of the nominal parameters for $T_{\rm eff}$ and log g for both stars (given in Table 2). For both stars these atmospheric parameters correspond to WD masses of 0.55 $M_{\odot}$, which according to an initial-final mass relationship for WDs (Cummings et al. 2018, their Figure 5), indicate the progenitor star masses were $\simeq$1 $M_{\odot}$, probably G-type stars.

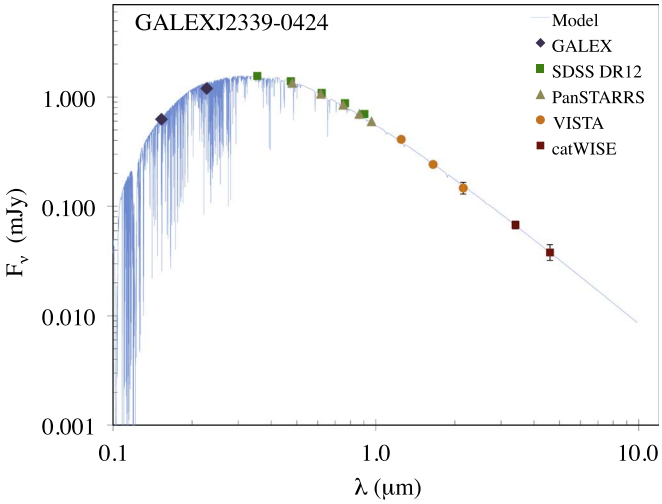

Figure 5. Spectral energy distribution for GALEXJ2339.

We explored uncertainties in $T_{\rm eff}$ and log g from the range of models that can fit within the error bars of the photometry fitting described above. However, the SDSS error bars are so small in our stars (<1%) that we found this method to result in unreasonably small errors ($\simeq$100 K) for the effective temperatures, which we know—from different modeling methods in the literature, and the changes seen over time from new developments in model structures, etc.—can have much larger uncertainties. Thus, we do not attempt to assign fitting errors to the atmospheric parameters. Instead we assume more typical uncertainties ($\sim$3% of the $T_{\rm eff}$ value) for He-dominated WDs in this $T_{\rm eff}$ range (Bergeron et al. 2011; Koester & Kepler 2015), choosing $\pm$ 500 K (to be conservative), with corresponding log g values consistent with fitting the photometry. Note that due to Gaia parallax constraints, uncertainties in log g are negligible. This results in lower and upper $T_{\rm eff}$/log g limits for GALEXJ2339 of 13235/7.84 and 14235/8.02, and for GD 378 of 15120/7.87 and 16120/7.98. See Appendix A for details on how we apply these limits.

Spectral energy distributions are given in Figures 5 and 6 with available photometry, and our best-fit models for each star are plotted in blue. The photometric data come from GALEX (Bianchi et al. 2017), SDSS (Alam et al. 2015), Pan-STARRS (Flewelling et al. 2020), 2MASS (Cutri et al. 2003), VISTA (McMahon et al. 2013), and catWISE (Eisenhardt et al. 2020) surveys. Spitzer fluxes for GD 378 are from Mullally et al. (2007). We checked the Spitzer archive at the position of GALEXJ2339, which at first returned a positive result suggesting that the WD may have been (unintentionally) observed in a prior field observation. Unfortunately, it turned out that GALEXJ2339 was just outside the imaged field of view. From Figures 5 and 6, we see that with the available data, neither WD displays evidence for an infrared excess due to circumstellar dust. Although early on it was recognized that heavy pollution and infrared excess are correlated (Jura 2008; Farihi et al. 2009), more recently it has been shown that only one in 30 polluted WDs exhibits an infrared excess when examined with Spitzer's 3–4 μm IRAC photometry (Wilson et al. 2019b). Even heavily polluted WDs do not always have detected infrared excesses (e.g., Klein et al. 2011; Raddi et al. 2015; Xu et al. 2017; Hoskin et al. 2020).

[15] http://lism.wesleyan.edu/LISMdynamics.html

[16] We apply the SDSS-to-AB magnitude corrections given in Eisenstein et al. (2006).

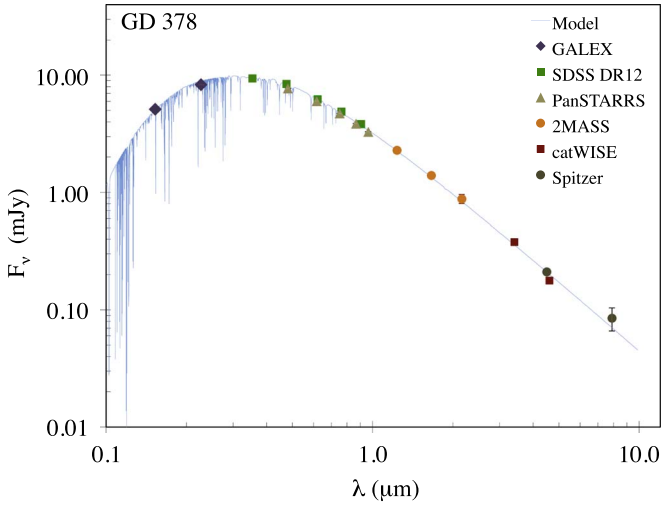

Figure 6. Spectral energy distribution for GD 378.

UV wavelengths are the most sensitive to the effects of interstellar reddening and line blanketing from heavy element pollution, both of which could cause the measured UV flux to be lower than predicted by a model without accounting for these factors. On the other hand if measured UV flux is much higher than the model, that would suggest that a higher-temperature model is needed to match the full SED. Both WDs in this study have GALEX photometry. As shown in Figures 5 and 6, our model spectra are well matched with the GALEX points of both stars, which lends support to the values derived from our model $T_{\rm eff}$/ log g fits with the assumption of negligible reddening.

5. Abundances

Our most noteworthy finding is that GALEXJ2339 and GD 378 have extraordinarily high Be abundances (relative to other rock-forming elements) compared with cosmic abundances and other heavily polluted WDs, as shown in Table 3. The full set of measured averaged abundances for all detected elements is given in Tables 4 and 5, with example model fits to portions of the spectra shown in Figure 7 for GALEXJ2339, and Figures 8 and 9 for GD 378. Abundances for major elements and upper limits for Be in the comparison WDs are given in Table 6. Details of our abundance fitting procedures are described in Appendix A.

For the comparison WDs, we re-examined a sample of heavily polluted WDs for which the authors have obtained high-quality HIRES spectra covering the 3130 Å region of the Be doublet. For most of these, we used previously published major element abundances and atmospheric parameters to derive Be upper limits from the spectra (see references in Table 6). However for two stars, PG1225−079 and SDSSJ1242 + 5226, we refit the atmospheric parameters with the inclusion of all elements in the atmospheric structure calculations. This resulted in lower $T_{\rm eff}$ by 1000 K for PG1225 and 2300 K for SDSSJ1242 + 5226 compared to previous studies (Klein et al. 2011; Raddi et al. 2015), and correspondingly altered abundance ratios. Since we only have a blue HIRES spectrum available for SDSSJ1242 + 5226, which does not cover the O I 7772 lines modeled by Raddi et al. (2015), we roughly estimated oxygen to have the same reduced abundance as other major elements compared to the analysis by Raddi et al. (2015). These changes in absolute abundances of a factor of 2 or 3 have very little effect on the relative abundances between elements (Klein et al. 2010), and are not important in our overall comparisons regarding the abundance of Be.

Table 3
Steady-state Beryllium Ratios Relative to CI Chondrites

WD name	Mg/Fe	Be/O	Be/Mg	Be/Si	Be/Fe
GALEXJ2339	1.4	121	190	191	267
GD 378	0.7	36	123	128	80
PG 1225-079	0.6	…	<33	<38	<20
GD 362	0.2	…	<23	<16	<5
SDSSJ1242+5226	1.4	<0.9	<6	<4	<8
SDSSJ0738+1835	1.0	<6	<6	<9	<6
G200−39	0.5	<187	<898	<639	<481
Ton 345	0.6	<122	<41	<27	<26
Sun	1.02	0.54	1.06	1.16	1.08
F and G stars (avg)	1.3	0.4	0.9	1.1	1.2
Bulk Earth	1.07	2.9	1.26	1.32	1.35

Note. Ratios are by number and relative to CI chondrite ratios from Lodders (2020). Abundances for GALEXJ2339 and GD 378 are from Tables 4 and 5, respectively, and comparison WD abundances are from Table 6. Values for the Sun are from Lodders (2020); F and G stars are from Boesgaard (1976a) and Reddy et al. (2003); and bulk Earth is from Allègre et al. (2001). The derived limits for G200−39 are not very restrictive, but they are included here as this WD accreted a Kuiper Belt analog, and we are showing that the upper limits do not preclude a beryllium overabundance in such an object. For the WDs, we adopt the steady-state values using diffusion timescales from the Montreal White Dwarf Database (MWDD; Dufour et al. 2017). Typical uncertainties on the measured Be ratios are about 50%. Note that both GALEXJ2339 and GD 378 have oxygen excesses as described in Section 5; thus, the Be/O ratios are somewhat less dramatic than those relative to Mg, Si, and Fe. If any WD system happens to be in an increasing phase of accretion, then all of its tabulated WD abundance ratios or upper limits would be larger by up to factors of two (see Section 5.1).

Figure 10 shows our model upper limit on the detection of the Be lines in the extremely heavily polluted WD, GD 362, as an example of how we derive the Be abundance upper limits for WDs in Table 6. Figure 10, Table 3, and panel (A) of Figure 11 demonstrate that the detections of Be in GALEXJ2339 and GD 378 are possible only because of the dramatic overabundance of Be in these stars, while a "normal" (chondritic) Be abundance is below our detection limit in even the most heavily polluted WDs with good S/N.

The masses of accreted material in the convection zones (CVZs) are calculated using Table 2 parameters ($M_{\rm WD}$ and fractional mass of the CVZ) and the measured abundance ratios for each element. Mass flux (flow rates), $\dot{M}$ (g s^{-1}), can then be derived using the CVZ pollution masses divided by the settling times from Tables 4 and 5. If accretion is ongoing, the calculated mass flux represents the accretion rate of material into the WD atmosphere. After accretion ends in WDs with relatively long settling times, heavy elements can continue to be observable in the WD photosphere for some time before they diffuse down out of sight (more on this in Section 5.1). In that situation, the mass flux can be more accurately thought of as the diffusion flux out of the base of the CVZ. Whatever the case, the total mass flow rates of $\dot{M} = 1.7 \times 10^9$ g s^{-1} for GALEXJ2339 and $\dot{M} = 1.8 \times 10^8$ g s^{-1} for GD 378 are normal for polluted WDs (compare Figure 3 of Xu et al. 2019).

Table 4
GALEXJ2339 Abundances and Parent Body Mass Compositions

Z	log(n(Z)/n(He))	n(Z)/n(He) (10^{-8})	$\sigma_{\rm spread}$ (10^{-8})	$\sigma_{T_{\rm eff}}$ (10^{-8})	n(Z)/n(O) (10^{-3})	τ(Z) (Myr)	% Mass Composition			
							Steady State	Rock Only No H_2O	Decreasing Phase	CI Chondrites
H	$-3.51^{+0.18}_{-0.31}$	31260	14430	7057	…	…				
Be	$-10.39^{+0.19}_{-0.34}$	0.0041	0.0010	0.0020	0.0136 ± 0.0068	2.47	3.9E-04	7.0E-04	2.2E-06	2.2E-06
O	$-5.52^{+0.04}_{-0.05}$	298.9	25.7	18.6	…	1.89	66.3	39.5	3.0	45.4
Mg	$-6.58^{+0.11}_{-0.14}$	26.4	4.0	6.0	88.4 ± 21.3	1.90	8.8	15.9	0.37	9.5
Si	$-6.59^{+0.07}_{-0.08}$	25.6	4.3	1.6	85.8 ± 16.0	1.90	9.9	17.9	0.43	10.8
Ca	$-8.03^{+0.26}_{-0.75}$	0.94	0.28	0.72	3.1 ± 2.4	1.27	0.78	1.4	3.2	0.88
Ti	$-9.58^{+0.21}_{-0.40}$	0.027	0.007	0.015	0.089 ± 0.049	1.15	0.029	0.052	0.52	0.045
Cr	$-8.73^{+0.16}_{-0.26}$	0.19	0.03	0.08	0.62 ± 0.25	1.18	0.21	0.39	2.6	0.26
Mn	$-9.03^{+0.16}_{-0.25}$	0.094	0.006	0.041	0.32 ± 0.12	1.17	0.12	0.21	1.4	0.19
Fe	$-6.99^{+0.18}_{-0.30}$	10.3	2.6	4.4	34.3 ± 15.7	1.22	12.3	22.1	85.8	18.6
Li	<-8.2	<0.6			<2.1	2.62	…	…	…	1.5E-04
Na	<-8.0	<1.0			<3.3	1.82	…	…	…	0.51
Al	<-7.7	<2.2			<7.5	1.85	0.74[a]	1.32[a]	<0.03	0.84
V	<-10.3	<0.0046			<0.015	1.14	…	…	…	5.4E-03
Ni	<-8.0	<1.0			<3.3	1.28	0.72[a]	1.30[a]	<2.6	1.10

Note. Abundances by number, n, and uncertainties, σ, as defined in Appendix A. Upper limits are from nondetections of Al I 3962 Å, V II 3125 Å, and Ni I 3515 Å. Uncertainties in Log abundances come from Equation (A1), and for n(Z)/n(O) are calculated according to Equation (A2). τ(Z) are the settling times in the WD atmosphere from the MWDD (Dufour et al. 2017). The compositions by mass in the four columns on the right are as follows (see also Section 5.1): "steady state" = accretion–diffusion equilibrium; "rock only" = the steady-state phase with "excess" O removed from the O abundance and attributed to water ice; "decreasing phase" = the decreasing phase after ∼7–8 Be settling times; "CI chondrites" = meteoritic abundances from Lodders (2020).
[a] Assumed contribution; see Section 5.2.

Table 5
GD 378 Abundances and Parent Body Mass Compositions

Z	log(Z/He)	n(Z)/n(He) (10^{-8})	$\sigma_{\rm spread}$ (10^{-8})	$\sigma_{T_{\rm eff}}$ (10^{-8})	n(Z)/n(O) (10^{-3})	τ(Z) (Myr)	% Mass Composition			
							Steady State	Rock Only No H_2O	Decreasing Phase	CI chondrites
H	$-4.48^{+0.12}_{-0.17}$	3311		1091	…	…				
Be	$-11.44^{+0.13}_{-0.19}$	0.00036	0.00007	0.00010	0.0040 ± 0.0014	1.07	1.2E-04	2.5E-04	2.2E-06	2.2E-06
C	$-7.35^{+0.15}_{-0.24}$	4.48	1.58	1.04	49.2 ± 23.3	0.91	2.4	4.9	0.12	4.1
O	$-6.04^{+0.18}_{-0.31}$	91.17	20.7	41.4	…	0.84	70.3	39.5	6.3	45.4
Mg	$-7.44^{+0.14}_{-0.20}$	3.67	0.50	1.26	40.2 ± 11.6	0.83	4.3	8.8	0.43	9.5
Si	$-7.49^{+0.09}_{-0.12}$	3.23	0.76	0.21	35.5 ± 18.0	0.78	4.7	9.6	0.76	10.8
P	$-9.35^{+0.20}_{-0.39}$	0.044	0.016	0.021	0.49 ± 0.2	0.68	0.081	0.17	0.044	0.10
S	$-7.81^{+0.19}_{-0.35}$	1.55	0.45	0.73	17.0 ± 6.2	0.65	3.1	6.3	2.5	5.4
Ca	$-8.70^{+0.26}_{-0.76}$	0.20	0.04	0.16	2.2 ± 1.0	0.55	0.59	1.2	3.0	0.88
Ti	$-10.13^{+0.22}_{-0.46}$	0.0073	0.0020	0.0044	0.081 ± 0.03	0.52	0.028	0.056	0.33	0.045
Cr	$-9.72^{+0.25}_{-0.68}$	0.019	0.0070	0.0134	0.21 ± 0.10	0.53	0.076	0.15	0.64	0.26
Mn	$-9.81^{+0.22}_{-0.46}$	0.015	0.0057	0.0084	0.17 ± 0.08	0.53	0.065	0.13	0.57	0.19
Fe	$-7.51^{+0.19}_{-0.36}$	3.12	0.33	1.72	34.3 ± 9.2	0.54	13.0	26.5	80.2	18.6
Li	<-7.5	<3.2			<34.7	1.15	…	…	…	1.5E-04
N[b]	<-7.3	<5.0			<55.0	0.86	…	…	…	0.25
Na	<-7.2	<6.3			<69.2	0.81	…	…	…	0.51
Al	<-7.7	<2.0			<22	0.79	0.56[a]	1.13[a]	<0.4	0.84
V	<-9.5	<0.03			<0.3	0.51	…	…	…	5.4E-03
Ni	<-8.3	<0.5			<5.5	0.54	0.77[a]	1.56[a]	<10	1.10

Notes. Similar to Table 4, but for GD 378. Upper limits are derived from nondetections of Li I 6708 Å, N I 1134 Å, Na I 5890 Å, Al II 3587 Å, V II 3125 Å, and Ni I 3515 Å. The compositions by mass in the four columns on the right are as follows (see also Section 5.1): "steady state" = accretion–diffusion equilibrium; "rock only" = the steady-state phase with "excess" O removed from the O abundance and attributed to water ice; "decreasing phase" = the decreasing phase after ∼6–7 Be settling times; "CI chondrites" = meteoritic abundances from Lodders (2020).
[a] Assumed contribution (see Section 5.2).
[b] Nitrogen upper abundance limit from FUSE. N is detected in an HST/COS spectrum (PI: B. Gänsicke) from which we derive an abundance of log(N/He) = −8.15 (see Section 5.2).

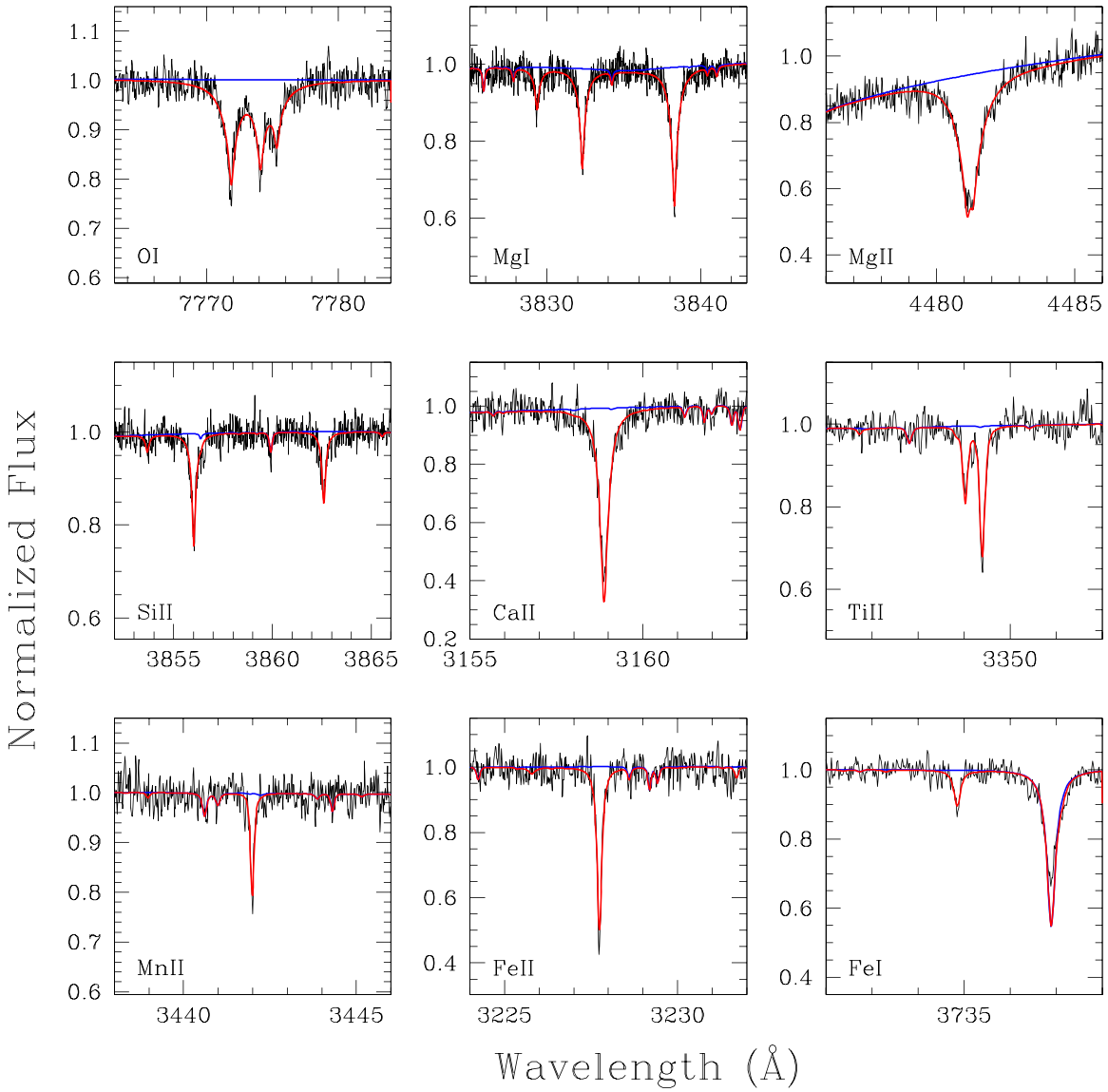

Figure 7. Portions of the Keck/HIRES spectrum of GALEXJ2339, displaying examples of each of the detected elements (along with Be from Figure 1). Wavelengths are in air and shifted to the laboratory frame of rest. The red line is our best-fit model, and the blue line is the same model with the abundance of the indicated element set to zero. In the lower right panel of Fe I, the stronger absorption line at 3736.9 Å is from Ca II.

Summing up the observed mass from elements heavier than He, we find the minimum masses of the parent bodies to be 9.4×10^{22} g for GALEXJ2339 and 4.5×10^{21} g for GD 378, comparable to some of the most massive solar system asteroids: 10 Hygiea (fourth most massive) and 7 Iris (16th most massive), respectively. The actual masses of the parent bodies could be much larger if accretion has been going on for more than a few settling times. These stars also have a lot of hydrogen, 4.4×10^{23} g and 7.7×10^{21} g for GALEXJ2339 and GD 378, respectively, but we do not know for sure how much H is associated with the current pollution, since, unlike the elements heavier than He, H tends to float to the top of the atmosphere, and accumulates from all accretion over time. We do know that the large amount of H in GALEXJ2339 is over the limit of the amount that could be primordial and preceding the DA-to-DB transition (otherwise the WD would never appear as spectral type DB dominated by optical He I lines) according to Rolland et al. (2020, their Figure 4). This implies that most of the H must have been accreted since that transition time (∼180 Myr ago for GALEXJ2339). The accretion of water-ice-rich bodies is the most likely explanation in such polluted WD systems with large amounts of H (Farihi et al. 2013; Raddi et al. 2015; Gentile Fusillo et al. 2017; Hoskin et al. 2020), consistent with our compositional analysis regarding oxygen excess in the two WDs studied here (Section 5.2 below).

5.1. Accretion–Diffusion

Relating the detected atmospheric abundances to the parent body composition depends on the interplay between accretion and diffusion in the system. Koester (2009) describes a three-phase model of increasing, steady-state, and decreasing abundances. In the increasing phase, settling is not yet playing a significant role, and the relative parent body abundances are directly the measured ones. For the steady state, we need to take into account the different settling times (τ(Z)) of the various elements using Equation (7) of Koester (2009) and τ(Z) from Tables 4 and 5. This effect can modify the observed

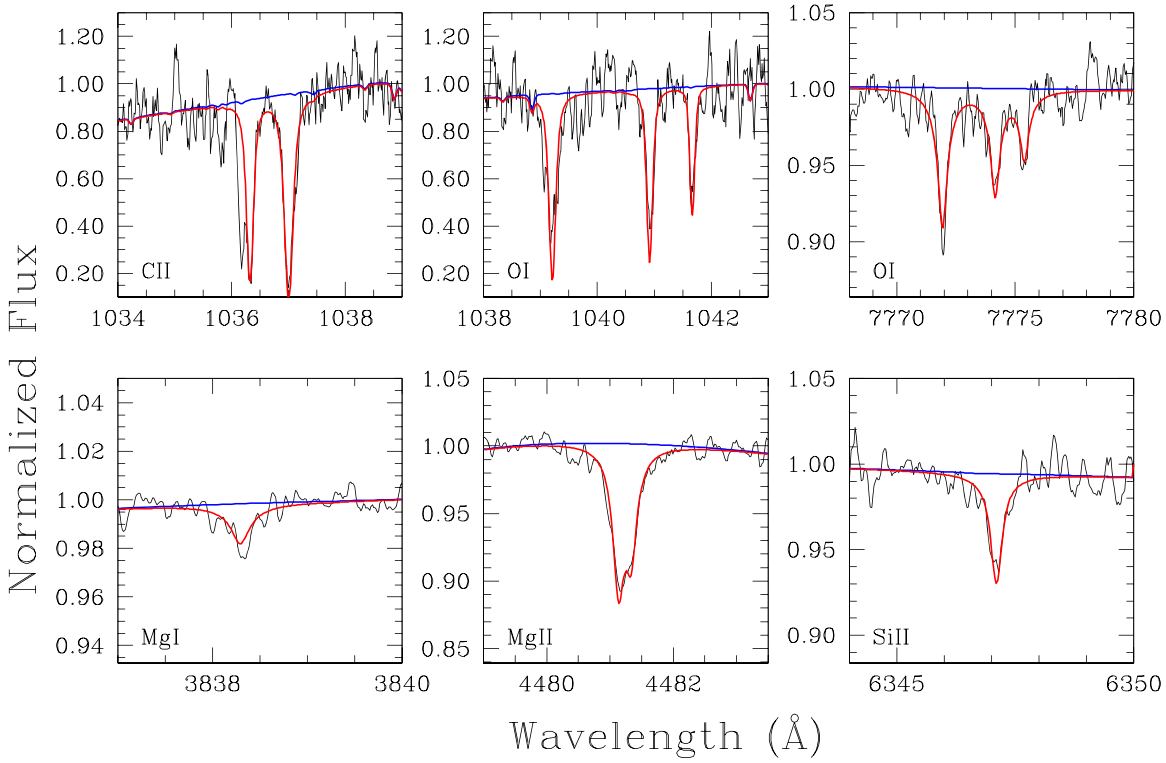

Figure 8. Portions of the FUSE (wavelengths less than 3000 Å in vacuum) and Keck/HIRES (wavelengths greater than 3000 Å in air) spectra of GD 378, displaying examples of each of the lighter detected elements up through Si (along with Be from Figure 2). The data are smoothed by a five-point average. The red and blue model lines have the same meaning as in Figure 7. Nonphotospheric components of C II 1036.34 Å and O I 1039.23 Å are present, blueshifted from the photospheric lines. These features are almost certainly interstellar (see Section 3.3).

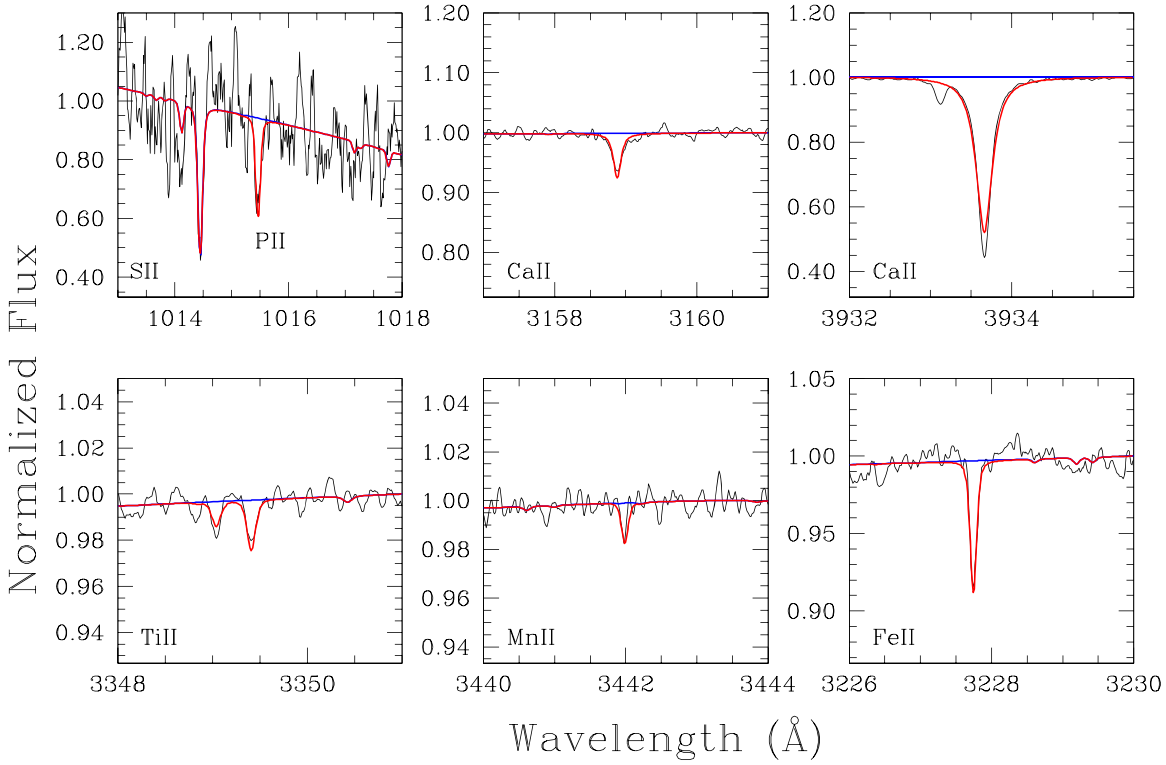

Figure 9. Continuation of Figure 8 for GD 378 elements P and heavier. Phosphorous and sulfur appear together in the upper left panel, where the stronger line at 1014.4 Å is from S II, and the line at 1015.5 Å is from P II. The absorption feature at 3933.1 Å is a blueshifted (most likely interstellar) component of the Ca II K-line (see Section 3.3).

Table 6
Beryllium Upper Limits and Major Element Abundances in Heavily Polluted WDs

WD Name	$T_{\rm eff}$	log g	[H/He]	[Be/He]	[O/He]	[Mg/He]	[Si/He]	[Fe/He]	Reference
PG 1225−079	9940	7.97	−3.98	<−12.0	…	−7.43	−7.50	−7.52	This paper
GD 362	10540	8.24	−1.14	<−10.7	<−5.14	−5.98	−5.84	−5.65	Z2007
SDSSJ1242+5226	10710	7.93	−3.77	<−11.0	∼−4.6	−5.68	−5.55	−6.11	This paper
SDSSJ0738+1835	13950	8.40	−5.73	<−10.0	−3.81	−4.68	−4.90	−4.98	D2012
G200−39	14490	7.95	−4.2	<−11.3	−6.62	−8.16	−8.03	−8.15	X2017
Ton 345	18700	8.00	−5.1	<−9.5	−4.58	−5.02	−4.91	−5.07	J2015

Note. Logarithmic abundances and upper limits by number. Be abundance upper limits are all newly derived in this work. Atmospheric parameters and abundances for O, Mg, Si, and Fe are from the papers listed in the reference column, except for the two that have been refit in this paper: PG 1225−079 (previously analyzed by Klein et al. 2011 and Xu et al. 2013), and SDSSJ1242+5226 (analyzed by Raddi et al. 2015; see also discussion in text Section 5). References are: Z2007 (Zuckerman et al. 2007); D2012 (Dufour et al. 2012); X2017 (Xu et al. 2017); and J2015 (Jura et al. 2015).

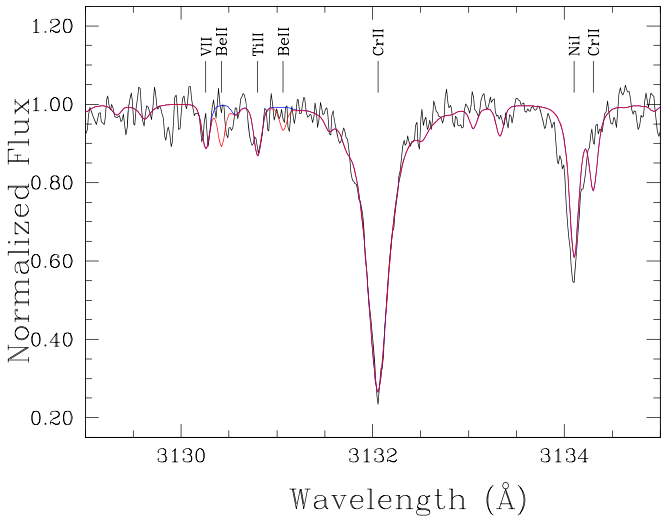

Figure 10. Be II region in GD 362, similar to Figure 1, but here no features coincident with the Be lines are detected. The red model line shows the Be upper abundance limit from Table 6.

abundance ratios by up to factors of two. We note that Figure 8 in Heinonen et al. (2020) shows that improved physics models can lead to diffusion timescale ratios that, for $T_{\rm eff} \lesssim 10{,}000$ K, are substantially different from those currently available and used in the present paper. However, those differences remain small in the $T_{\rm eff} \sim 13{,}000$–$16{,}000$ K regime of the two Be-enriched WDs, so this uncertainty does not affect our conclusions in any way.

Koester (2009) has modeled the start of the decreasing phase by switching accretion off, at which point the heavy elements begin differentially settling in the WD atmosphere according to an exponential decay governed by their relative diffusion times. We use this approach here, as it is sufficiently illustrative for the current paper, but we note that a somewhat more elaborate model includes an exponential decay of the accretion from the disk as described by Jura et al. (2009), and employed by Doyle et al. (2020, 2021).

The WDs studied here have settling times of the order 10^5–10^6 yr, which is in the estimated range of disk lifetimes (Girven et al. 2012; Veras & Heng 2020); thus, at the outset, it is possible for us to interpret these systems to be in any one of the three phases. A detected dust disk would narrow down the possibilities—to increasing phase or steady state—but, as shown in Figures 5 and 6, neither GALEXJ2339 nor GD 378 have a detected infrared excess. Decreasing phase abundances can differ significantly from the original parent body composition as the element ratios undergo an exponential decay over time since the end of accretion. As, aside from H, the lightest detected element, Be, has the longest dwell time compared to the other elements in the WD atmosphere, it is natural to ask, can a decreasing phase explain the large overabundance of Be?

We calculated the number of e-folding settling times it would take to have a Be percent mass composition—which began as chondritic—evolve into what is observed today. For both stars, it would take about seven to eight Be settling times (∼15 Fe settling times) to achieve the two orders of magnitude overabundance of mass composition of Be seen in the WD atmospheres. However, such a scenario also results in abundance patterns for the other elements that are extreme (see column "decreasing phase" in Tables 4 and 5), requiring parent body compositions that are ≃80% Fe, with ≃3%–6% O, ≃3% Ca, <1% in each of Mg, Si, and Al, all with a chondritic proportion of Be. This bizarre makeup, together with the fact that for GALEXJ2339 after seven to eight settling times the mass of the polluting parent body would need to have started out more than three (probably closer to ten) times the mass of planet Earth, makes the decreasing phase a highly unlikely explanation for the large overabundance of Be in the two WDs. A thorough and quantitative treatment of the accretion–diffusion situation, and consideration of multiple accretion events, is presented in the companion to this paper by Doyle et al. (2021).

As mentioned above, the abundance ratios between the increasing phase and the steady state are quite similar, differing by at most a factor of 2. In the following analysis, for simplicity, we consider only the steady-state values, which is a conservative approach in this situation where we are dealing with the overabundance of lighter elements (longer settling times) compared to the other elements associated with the polluting planetary material.

5.2. Oxygen Excesses

Besides the huge overabundance of Be, and large amounts of H, O is overabundant in both WDs as well. From Tables 4 and 5, one finds that the number of O atoms is much greater than that required to bond with the other major rock-forming elements (Mg, Si, and Fe), as detailed in the following paragraph. Two principle mechanisms can be responsible for excess O: (1) the system may be in a settling phase that makes O appear overabundant; or (2) there was water in the accreted parent body. We have already noted that a long-time declining phase is unlikely; it would take at least four Be settling times,

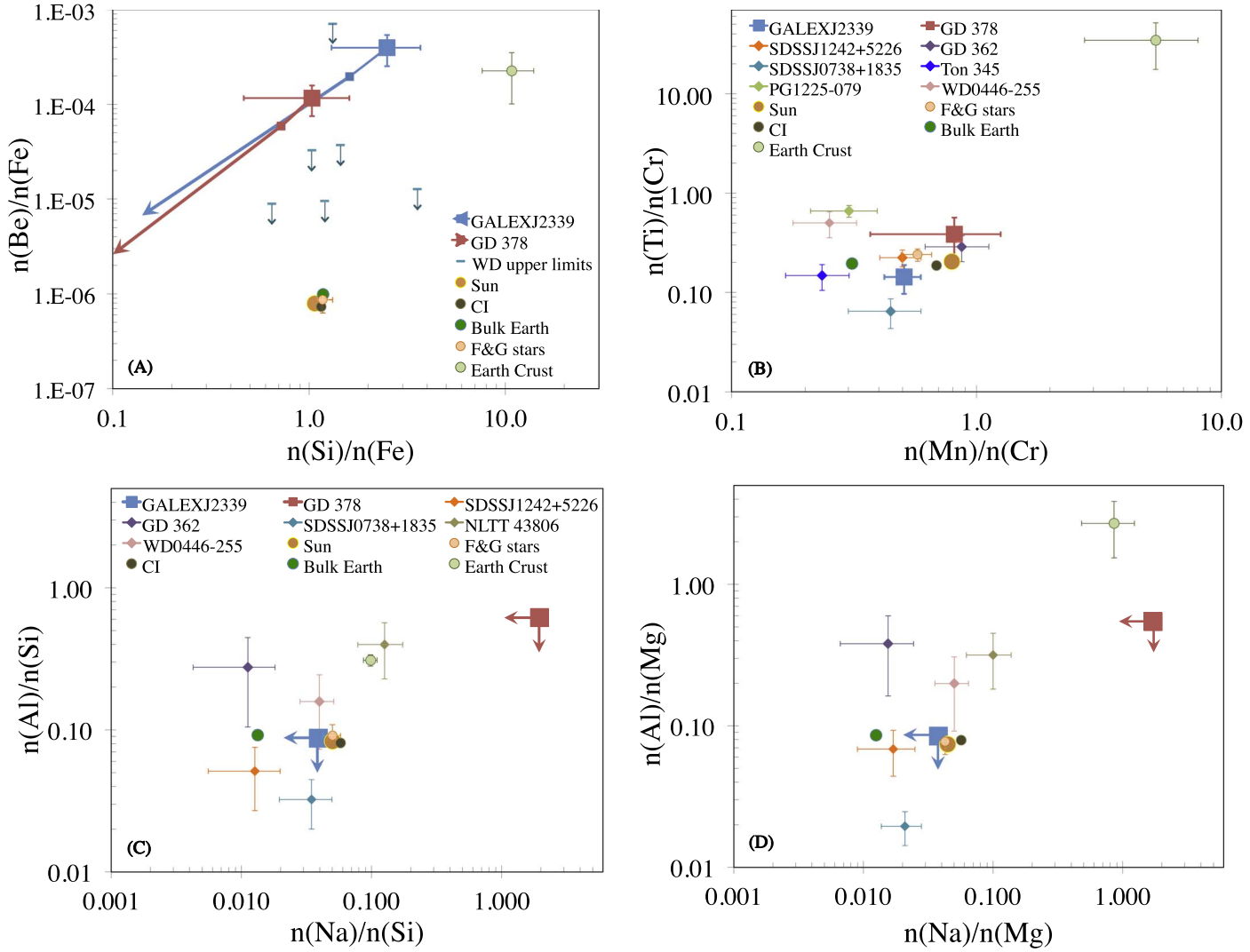

Figure 11. Abundance ratios by number. Large filled squares with error bars and/or upper limits are observed photospheric abundances in the two Be WDs, while the small squares in panel (A) mark the steady-state values. Following Swan et al. (2019), we used backward time arrows to chart how the diffusion evolution would look if the systems are in a decreasing phase. The arrow head positions denote what the starting abundance ratios would have been if accretion ceased approximately four Be settling times ago (about 10 Myr for GALEXJ2339 and 4 Myr for GD 378). In panels (B), (C), and (D), differential diffusion has almost no effect on the displayed ratios due to similar settling times of the plotted elements; these ratios are nearly independent of the accretion–diffusion states of the systems. In panels (C) and (D), the arrows on GALEXJ2339 and GD 378 indicate upper abundance limits, and symbols in panel (D) are the same as those defined in panel (C). Filled circles are F- and G-type stars (Be from Boesgaard 1976a; all other elements from Reddy et al. 2003), solar and CI chondrites (Lodders 2020), bulk Earth (Allègre et al. 2001), and Earth's crust (Rudnick & Gao 2003). WD upper limits for Be are from Table 6 and are uncorrected for settling. Other WD abundances, uncorrected for settling, are from: SDSSJ1242 + 5226 (this paper), GD 362 (Zuckerman et al. 2007), SDSSJ0738 + 1835 (Dufour et al. 2012), Ton 345 (Jura et al. 2015), PG 1225−079 (Xu et al. 2013), WD 0446−255 (Swan et al. 2019), and NLTT 43806 (Zuckerman et al. 2011).

∼10 Myr and ∼4 Myr in GALEXJ2339 and GD 378, respectively, to account for their oxygen excesses. By that point, the ratios of the other elements become unlike any understandable abundance pattern. We also pointed out that the large H abundance in these types of WDs implies the accretion of water, so next we evaluate that scenario.

We use the $n(Z)/n(\mathrm{O})$ abundance ratios to calculate oxygen budgets to get a measure of the partitioning of O in rocky material. As described in Klein et al. (2010), we count up the number of O atoms that can be carried by the major and minor oxides in a rocky body: MgO, Al_2O_3, SiO_2, CaO, FeO, and NiO.[17]

[17] Oxides from trace elements (Na_2O, P_2O_5, TiO_2, V_2O_5, Cr_2O_3, and MnO) can be included, but in practice their contributions to the oxygen budget are negligible.

Being among the top seven most abundant elements in bulk Earth, Al and Ni are expected to be non-negligible in a total parent body composition at the level of one to a few percent, but we only have upper limits on their observed abundances. Therefore in calculating the percent mass compositions and oxygen budgets, we assume values for Al and Ni as associated with their partner elements, Ca and Fe, respectively. That is, for the increasing and steady-state accretion phases, we set the Al and Ni abundances to CI chondrite ratios (similar to the Sun and bulk Earth) at $\mathrm{Al/Ca} = 0.94$ and $\mathrm{Ni/Fe} = 0.058$, by mass, since Al/Ca and Ni/Fe have similar behaviors in rocky bodies based on their condensation temperatures and tendencies to be in a metallic form or not.

For both GALEXJ2339 and GD 378, we find that in the steady state, just one-third of the detected O atoms could have been delivered in the form of rocky oxides. There is far more

than enough hydrogen in the convection zones of these WDs to account for the excess O to be associated with H_2O ice. After subtracting the excess O from its total abundance, except for Be, the remaining overall mass composition patterns are remarkably similar to chondritic (see columns "rock only no H_2O" and "CI chondrites" in Tables 4 and 5). Considering relative proportions, the parent bodies polluting both WDs each contained roughly comparable amounts (by mass) of rock and water ice. That, along with the observation of other volatile species in the FUSE spectrum of GD 378, namely C and S, leads us to conclude that the parent bodies that polluted these WDs were composed of material that originated beyond the ice-lines of their protoplanetary disks.

We note that an archival HST/COS spectrum of GD 378 (program #12474) contains photospheric lines of N (B. Gänsicke, private communication), which is consistent with the results that we have established here. GD 378 is the second WD known to display N from planetary accretion; G200−39 was the first (Xu et al. 2017). Referring to the footnotes in Table 5, the N abundance we derive from the COS spectrum is $\log(\mathrm{N/He}) = -8.15$, which translates to a steady-state mass composition for N of 0.5% (or 1.0% of the rocky material without H_2O). These percentages may be compared to 0.25% in CI chondrites (Lodders 2020), 1.5% in comet Halley's dust (Jessberger et al. 1988), and ≃2% in the Kuiper Belt analog accreted by G200-39 (Xu et al. 2017).

5.3. Comparison to Li-polluted WDs

Two recent papers have reported the discovery of lithium in a handful of very cool ($T_{\rm eff} < 5000$ K) WD atmospheres (Kaiser et al. 2021; Hollands et al. 2021). The Li abundances appear modestly enhanced in all of the stars. Kaiser et al. (2021) interpreted the enhanced Li in these old WDs in the context of galactic chemical evolution, while Hollands et al. (2021) asserted that the observed Li in all four of their sample stars comes from differentiated planetary crusts. Indeed, the elements Li and Be are enhanced in Earth's crust, but we also note that the overall composition of the crust is considerably different from bulk Earth, CI chondrites, and main-sequence stars. It is dominated by O, Si, Al, and Ca, enhanced in elements such as Li, Be, Na, Mn, and Ti, while depleted in elements such as Fe, Mg, and Cr. We have already pointed out in the preceding section that the rocky portions of both parent bodies have similar overall abundance patterns as CI chondrites, but since we have measured suites of elements in both the Be WDs, we can evaluate some of the element ratios in more detail. See also Doyle et al. (2021) for additional analysis of parent body compositions.

DB type WDs are generally too warm to allow for the detection of easily ionizable elements such as Li and Na, but nonetheless we derive their upper limits (Tables 4 and 5). A combination of the heavy pollution and cooler temperature of GALEXJ2339 yields an upper limit of Na that is close to chondritic, while in GD 378, the Na limit is much less constrained. For lithium, the upper limits are near or much higher than the overabundances observed for Be in the two stars: in GALEXJ2339, the steady-state Li/Mg upper limit is ≃300 times the chondritic ratio, while in the case of GD 378, it is more than 5000 times chondritic. Thus it is possible that Li may also be extremely overabundant in either or both of GALEXJ2339 and GD 378, but we are simply not able to measure it with current observations.

In Figure 11, panel (A) shows how the Be/Fe ratios may be compared to Earth's crust, but the Si/Fe ratios do not agree. In panel (C), the unique similarity with the Earth crust ratios is apparent for NLTT 43806, whose Al-rich abundance pattern has been interpreted as originating from a parent body containing a significant amount of crust (Zuckerman et al. 2011). The other WDs do not display such a pattern, and combined with the comparisons shown in panels (B) and (D), it is clear that the abundances of the two Be WDs are not at all similar to planetary crust material. Rather, apart from the Be overabundance, the element ratios and rocky mass compositions of these two WD are, by and large, consistent with chondritic.

6. Discussion and Conclusions

Ann Merchant Boesgaard has spearheaded studies of light element abundances in stars in the solar vicinity. Summaries can be found in Boesgaard (1976b) and Boesgaard et al. (2020). The primary production mechanism for boron and beryllium is generally thought to be spallation by cosmic rays on elements such as oxygen, carbon, and nitrogen in the ISM. For lithium, production by spallation is important, but not necessarily the dominant production process. Abundances of lithium, beryllium, and boron in young main-sequence stars are typically comparable to or greater than abundances in older main-sequence stars. Li abundances are enhanced in a few post-main-sequence stars, but this has never been found to be the case for beryllium; Be abundances are always reduced by stellar evolution.

Table 3 in Boesgaard (1976a) gives mean Be abundances by number relative to H in main-sequence G- and F-type stars (including the Sun) equal to 1.3×10^{-11}. Boesgaard remarks that, within the errors, the meteoritic value agrees with the solar value and that 1.3×10^{-11} is the cosmic Be abundance. Table 2 in Boesgaard (1976a) contains 38 G- and F-type stars, none of which have a Be abundance more than a factor of 2 above solar. A mostly independent set of stars is plotted in Figure 5 of Boesgaard et al. (2004) where the most Be-rich stars have Be abundances that are again within a factor of 2 of solar and agree with the meteoritic value.

Much larger downward deviations from the mean are found in some main-sequence F-type stars with temperatures in the range 6400–6800 K; by Hyades age, Be can be depleted by up to a factor of 6 (Boesgaard et al. 2020). The progenitors of many white dwarfs are such F-type stars.

Given the above, we conclude that the excess of Be in GD 378 and GALEXJ2339 is a signature of an environment where O and/or C, N, and protons were subjected to MeV collisions, either direct (accelerated protons) or reverse (accelerated O and/or C, N), resulting in unusually efficient production of Be by spallation. The high collisional energy was presumably the result of proximity to the source of energetic particles and a stopping distance comparable to the scale of the target. One possibility is that the star and planetesimal formation may have occurred in an environment containing a strong source of high-energy radiation. If the high-energy source were interior to the disk, i.e., the star itself, then the irradiated gas would likely be sufficiently close to the star that planetesimals formed out of the gas would be relatively dry (unlike the ice-rich bodies found here), and could not survive the evolution of the star unless they migrated to larger semimajor axes. Also, if irradiated gas with a high Be abundance located close to a

star were to accrete onto the outer layers of that star, then one might expect to see at least some young stars with supersolar Be abundances. But no such stars have been discovered in the Pleiades and αPer clusters (e.g., Boesgaard et al. 2003).

The foregoing assumes a quiescent protoplanetary disk, but different scenarios could occur in more dynamic disks, such as those with magnetically driven outflows. Magnetocentrifugal winds can potentially transport thermally processed irradiated material from inner to outer regions of a protoplanetary disk (e.g. Shu et al. 1997; Giacalone et al. 2019), where it may become incorporated into planetesimals formed at those locations. On the other hand, if the source was external to the progenitor (for example, a nearby Wolf–Rayet star), then it could irradiate the outer gaseous portions of a protoplanetary disk before rocky planetesimals were fully formed. In either of the last two scenarios, such planetesimals then could have survived until the star evolved into a white dwarf, and would potentially contain significant amounts of water ice, as found in the objects studied here.

An alternative model to explain the high Be abundance is presented in the accompanying paper by Doyle et al. (2021). Whatever the case, if the measured high Be abundance is due to a spallation process of any sort, then one also anticipates enhanced lithium and boron abundances.

More generally, this remarkable detection of Be suggests that, especially with the next generation of large telescopes, additional elements may be added to Table 1, providing new insights into processes associated with planetary formation and/or evolution. For example, an observation of barium in a polluted WD could inform us about the presence (or lack of) plate tectonics in an extrasolar planetary body as predicted by Jura et al. (2014).

This paper is dedicated to the memory of Michael Jura, who was a pioneer and leader in the study of polluted white dwarfs, especially in the context of measuring and understanding the compositions of extrasolar minor planets. Fittingly, asteroid 6406 Mikejura (https://ssd.jpl.nasa.gov/sbdb.cgi?sstr=6406;orb=1) was named after him.

We thank the anonymous referee for a helpful report that improved the manuscript. This paper has benefited from conversations with Detlev Koester, Boris Gänsicke, Jay Farihi, Geoff Marcy, and Ted Johnson. We are grateful to Boris Gänsicke for kindly giving us permission to discuss the unpublished detection of photospheric N in GD 378's COS spectrum. We also thank Diego Romani for assisting with the optical spectrum of GD 378 and Lou Baya Ould Rouis for help with observing planning.

B.K. was supported in part by the M. Hildred Blewett Fellowship of the American Physical Society, www.aps.org. A.D. and B.K. acknowledge support from the NASA Exoplanets program award No. 80NSSC20K0270 (EDY). Partial support was also provided by other NASA grants to UCLA. S. B. acknowledges support from the Laboratory Directed Research and Development program of Los Alamos National Laboratory under project No. 20190624PRD2. C.M. and B.Z. acknowledge support from NSF grants SPG-1826583 and SPG-1826550.

Some of the data presented herein were obtained at the W.M. Keck Observatory, which is operated as a scientific partnership among the California Institute of Technology, the University of California and NASA. The Observatory was made possible by the generous financial support of the W. M. Keck Foundation. We recognize and acknowledge the very significant cultural role and reverence that the summit of Maunakea has always had within the indigenous Hawaiian community.

This work has made use of data from the European Space Agency (ESA) mission Gaia (https://www.cosmos.esa.int/gaia), processed by the Gaia Data Processing and Analysis Consortium (DPAC, https://www.cosmos.esa.int/web/gaia/dpac/consortium). Funding for the DPAC has been provided by national institutions, in particular the institutions participating in the Gaia Multilateral Agreement.

This publication makes use of data products from the Two Micron All Sky Survey, which is a joint project of the University of Massachusetts and the Infrared Processing and Analysis Center/California Institute of Technology, funded by NASA and the National Science Foundation. The following atomic spectral line databases were consulted: Vienna Atomic Line Database (VALD), Kurucz (1995, R. L. Kurucz and B. Bell, CD-ROM No. 23, Cambridge, MA: Smithsonian Astrophysical Observatory), NIST Standard Reference Database 78, and van Hoof (2018).

Appendix A
Absorption Line Measurements and Abundance Fitting

Equivalent widths (EWs) and line center positions are measured with the IRAF task, *splot*, by fitting a Voigt function to the line profiles, and also by direct flux summation for unblended lines. The quoted values in Tables 7 and 8 are calculated from an average of three separate measurements with different continuum ranges. For the uncertainties, we combine the standard deviation of the three EW measurements with the average *splot* profile-fitting uncertainty in quadrature.

The abundances are extracted as follows. For a range of effective temperatures, surface gravities, and [H/He] abundances, we varied the abundances of all of the other detected elements in steps of 0.5 dex. We use the Vienna Atomic Line Database (VALD) for the atomic data of each line.[18] This provides us with a grid of model atmospheres and synthetic spectra that we then interpolate to fit the final abundances. We follow an approach similar to that described in Dufour et al. (2012) and divide the observed spectra into 5–10 Å segments that are centered around the spectral lines that we want to fit. For each of those segments, we use a χ^2 minimization algorithm to find the abundance that yields the best fit to the line(s) present in the segment. Only one element at a time is fitted in each segment, and most elements are fitted in more than one segment. Two contributions dominate the uncertainty on the absolute abundances: the uncertainty on $T_{\rm eff}$ and the spread between abundances derived for different segments. The first contribution is obtained by performing the fitting procedure at $T_{\rm eff} \pm \sigma(T_{\rm eff})$, and the second contribution is estimated by taking the standard deviation of the mean from the different abundance measurements. If an element only appears in one or two segments, then the "spread" error is estimated by inspection of model fits at varied higher and lower abundances.

It has been shown that the element-to-element ratios are much less sensitive to variations in $T_{\rm eff}/\log g$ than are the absolute abundances (Klein et al. 2010, 2011). Nonetheless, we want to estimate both the absolute and relative abundance dependence on $T_{\rm eff}/\log g$.[19] But first, some comments on

[18] Atomic line data for the well-studied Be lines are almost identical in other atomic databases, Kurucz, NIST, and van Hoof (2018).

[19] Note that $T_{\rm eff}$ and $\log g$ are themselves linked through the flux-solid angle formula used in photometric-parallax fitting. That is, with the distance fixed, a hotter model requires a smaller $R_{\rm WD}$ (larger $M_{\rm WD}$, i.e., larger $\log g$) to fit the photometry (see, e.g., Equation (1) of Coutu et al. 2019).

Table 7
Absorption Lines in GALEXJ2339

Ion	λ (Å)	EW (mÅ)	Ion	λ (Å)	EW (mÅ)
Be II	3130.42	85 ± 12	Ti II	3341.88	22 ± 3
Be II	3131.07	49 ± 10	Ti II	3349.04	31 ± 3
O I	7771.94	283 ± 8	Ti II	3349.41	62 ± 3
O I	7774.16	194 ± 14	Ti II	3361.22	53 ± 3
O I	7775.39	172 ± 21	Ti II	3372.80	45 ± 3
O I	8447	348 ± 24	Ti II	3383.77	29 ± 4
Mg I	3829.35	52 ± 14	Ti II	3685.20	30 ± 4
Mg I	3832.30	156 ± 6	Ti II	3759.29	24 ± 4
Mg I	3838.29	255 ± 17	Ti II	3761.32	23 ± 4
Mg I	5167.32	25 ± 7	Cr II	3120.36	50 ± 4
Mg I	5172.68	62 ± 3	Cr II	3124.97	79 ± 7
Mg I	5183.60	85 ± 9	Cr II	3132.05	89 ± 16
Mg II	4481	541 ± 46	Cr II	3197.08	20 ± 4
Mg II	7877.05	137 ± 60	Cr II	3358.49	22 ± 3
Mg II	7896.20	369 ± 59	Cr II	3368.04	34 ± 2
Si II	3856.02	108 ± 4	Cr II	3408.76	20 ± 2
Si II	3862.59	66 ± 5	Cr II	3422.73	24 ± 3
Si II	4128.05	40 ± 11	Mn II	3441.99	37 ± 2
Si II	4130.89	53 ± 7	Mn II	3460.31	21 ± 5
Si II	5041.02	30 ± 6	Fe I	3570.10	20 ± 3
Si II	5055.98	73 ± 27	Fe I	3581.19	34 ± 3
Si II	6347.11	202 ± 7	Fe I	3734.86	22 ± 3
Si II	6371.37	99 ± 6	Fe I	3749.49	20 ± 2
Ca II	3158.87	306 ± 14	Fe II	3154.20	54 ± 7
Ca II	3179.33	352 ± 28	Fe II	3167.86	38 ± 9
Ca II	3181.28	45 ± 4	Fe II	3177.53	25 ± 5
Ca II	3706.02	104 ± 13	Fe II	3186.74	32 ± 8
Ca II	3736.90	178 ± 7	Fe II	3192.91	24 ± 9
Ca II	3933.66	1409 ± 94	Fe II	3193.80	41 ± 10
Ca II	3968.47	1053 ± 156	Fe II	3196.07	30 ± 6
Ca II	8498.02	100 ± 17	Fe II	3210.44	57 ± 4
Ca II	8542.09	587 ± 34	Fe II	3213.31	84 ± 5
Ca II	8662.14	349 ± 17	Fe II	3227.74	120 ± 6
Ti II	3190.87	22 ± 6	Fe II	3247.18	20 ± 7
Ti II	3234.51	47 ± 5	Fe II	3259.05	24 ± 4
Ti II	3236.57	28 ± 3	Fe II	4923.92	27 ± 9
Ti II	3239.04	20 ± 5	Fe II	5018.44	42 ± 6
Ti II	3241.98	26 ± 6	Fe II	5169.03	66 ± 4

Note. Observed lines with measured EW >20 mÅ. Wavelengths are in air.

Table 8
Absorption Lines in GD 378

Ion	λ (Å)	EW (mÅ)	Ion	λ (Å)	EW (mÅ)
Be II	3130.42	8.6 ± 1.8	Si III	1113.23	66 ± 12
Be II	3131.07	3.8 ± 1.6	P II	1015.46	49 ± 10
C II	1009.86	22 ± 7	P II	1154.00	38 ± 13
C II	1010.08	31 ± 7	S II	1014.11	34 ± 9
C II	1010.37	63 ± 12	S II	1014.44	63 ± 9
C II	1036.34	146 ± 24	S II	1019.53	48 ± 12
C II	1037.02	236 ± 57	S II	1124.99	45 ± 15
O I	988.66	104 ± 37	Ca II	3158.87	16 ± 3
O I	988.77	*blended*	Ca II	3179.33	16 ± 2
O I	990.13	124 ± 47	Ca II	3736.90	5.6 ± 0.6
O I	990.20	*blended*	Ca II	3933.66	165 ± 2
O I	999.50	110 ± 21	Ca II	3968.47	96 ± 2
O I	1039.23	207 ± 57	Ti II	3349.03	1.9 ± 0.7
O I	1040.94	130 ± 19	Ti II	3349.40	2.3 ± 0.5
O I	1041.69	80 ± 16	Cr II	3120.40	3.6 ± 1.1
O I	1152.15	171 ± 17	Cr II	3124.97	4.7 ± 1.2
O I	7771.94	46 ± 8	Cr II	3132.05	3.6 ± 0.8
O I	7774.16	35 ± 14	Mn II	3441.99	1.3 ± 0.4
O I	7775.39	19 ± 5	Fe II	1063.18	59 ± 16
O I	8447	142 ± 24	Fe II	1068.35	31 ± 10
Mg I	3838.29	8.6 ± 2.0	Fe II	1144.94	63 ± 12
Mg II	4481	62 ± 14	Fe II	1148.28	60 ± 20
Si II	992.68	355 ± 39	Fe II	3154.20	8.3 ± 1.6
Si II	992.70	*blended*	Fe II	3167.86	3.2 ± 1.0
Si II	1020.70	98 ± 21	Fe II	3210.44	4.2 ± 0.7
Si II	3856.02	10.7 ± 1.8	Fe II	3213.31	7.5 ± 1.6
Si II	3862.59	5.8 ± 0.9	Fe II	3227.74	12 ± 2.0
Si II	4130.89	8.4 ± 2.7	Fe II	5169.03	7.7 ± 1.9
Si II	6347.11	37 ± 7	Fe III	1122.52	42 ± 8
Si II	6371.37	12 ± 2	Fe III	1124.88	52 ± 13
Si III	1109.97	31 ± 12	Fe III	1126.729	50 ± 24

Note. Si II λ989.87 and Fe II λ989.90 are blended with a combined EW of ≃ 200 mÅ; similarly O I λ990.80 and Fe II λ990.86 have a blended EW of ≃ 180 mÅ. These transitions are not used in the abundance analysis. Wavelengths are in vacuum below 3000 Å, and air above 3000 Å.

dealing with abundances in log-space versus number-space are in order. When discussing absolute abundances of elements that can be anywhere between one and 11 orders of magnitude less abundant than the dominant atmospheric element (H or He), it is certainly convenient to use logs: $[Z/H(e)] = \log_{10}[n(Z)/n(H(e))]$. However, if one has to convert a log uncertainty to number-space, the resulting uncertainties will be asymmetric about the nominal number abundance. This can cause difficulties in error propagation if one wishes to calculate a quantity in number-space, particularly those involving element-to-element ratios such as an oxygen budget or fugacity (Doyle et al. 2019, 2020). In our model fitting, we measure the element abundances in number-space, $n(Z)/n(H(e))$, and we also calculate the spread uncertainties in number-space as described in the preceding paragraph. Thus, here we choose to report abundances and their symmetric uncertainties in number-space (which translates to asymmetric uncertainties in log-space).

To separate the model-dependent (i.e., $T_{\rm eff}$/ log g) uncertainty contributions from those of spectral measurements, in Tables 4 and 5, we give abundances with the associated contributions from the spread error $\sigma_{\rm spread}$ and the error from varying the temperature, $\sigma_{T_{\rm eff}}$, listed separately. This way, the uncertainties on relative element abundances can be computed by propagating the uncertainties on the individual element abundances while taking care to remove the correlated portion of the uncertainty related to $T_{\rm eff}$, according to Equation (A2).

Explicitly, for general Z_i and Z_j, the element-to-element abundance ratios, $n(Z_i)/n(Z_j)$, are obtained directly from the $n(Z_i)/n(\mathrm{He})$. Continuing to work in number-space but dropping the "$n()$" for simplicity, the total uncertainty on the absolute abundance Z_i/He is just a propagation of the independent uncertainty contributions, $\sigma_{\rm spread}$ and $\sigma_{T_{\rm eff}}$:

$$\sigma_{\rm tot}\left(\frac{Z_i}{\mathrm{He}}\right) = \left(\sigma^2_{\rm spread}\left(\frac{Z_i}{\mathrm{He}}\right) + \sigma^2_{T_{\rm eff}}\left(\frac{Z_i}{\mathrm{He}}\right)\right)^{1/2}, \qquad \text{(A1)}$$

and the uncertainty in the ratio Z_i/Z_j may be calculated as:

$$\frac{\sigma\left(\frac{Z_i}{Z_j}\right)}{\left(\frac{Z_i}{Z_j}\right)} = \left(\left(\frac{\sigma_{\rm spread}\left(\frac{Z_i}{\rm He}\right)}{\left(\frac{Z_i}{\rm He}\right)}\right)^2 + \left(\frac{\sigma_{\rm spread}\left(\frac{Z_j}{\rm He}\right)}{\left(\frac{Z_j}{\rm He}\right)}\right)^2 + \left(\frac{\sigma_{T_{\rm eff}}\left(\frac{Z_i}{\rm He}\right)}{\left(\frac{Z_i}{\rm He}\right)} - \frac{\sigma_{T_{\rm eff}}\left(\frac{Z_j}{\rm He}\right)}{\left(\frac{Z_j}{\rm He}\right)}\right)^2\right)^{1/2}, \quad \text{(A2)}$$

where the third term on the right-hand side accounts for the fact that the set of element abundances predominantly move together, up and down, with variations in $T_{\rm eff}/\log g$.

This kind of treatment assumes that the dominant abundance uncertainty comes from line measurement and modeling variations, but we are aware that there are systematic uncertainties that can be contributing to the measurements in a nonstatistical way. For example, the observation of self-reversed core inversions in the He I 5876 profile of DB WDs suggests that there may be some problems with model temperature calibrations, possibly because of missing physics such as 3D effects, convective overshoot, and non-LTE effects (Klein et al. 2020). Also, discrepancies between UV and optical abundances noted for various stars (e.g., Gänsicke et al. 2012; Xu et al. 2019) may be due to uncertain atomic data (Vennes et al. 2011).

Appendix B
Model Checks from Abundances

In GD 378, three elements (O, Si, and Fe) are detected in both FUSE (UV) and HIRES (optical) data, so we began by analyzing those spectra separately to check for possible UV versus optical abundance discrepancies. Referring to Table 9, the UV and optical abundances derived for these three elements agree within the uncertainties. Given the UV-optical consistency for these three major elements, we proceeded with our abundance analysis on the combined HIRES + FUSE spectrum, generating a single model that incorporates the fits to all observed lines.

We also checked the ionization balance, i.e., the degree of agreement in abundances derived from different ionization states of the same element. For GD 378, the total Mg abundance, as derived separately from lines of Mg I and Mg II, only differs by 27% at the nominal model temperature, which is similar to what we find with the cooler model (23%) and somewhat worse (45%) from the hotter model. Likewise, the discrepancies between the total Fe abundance from Fe II and Fe III are only 14%, 11%, and 10% from the cool, nominal, and hot models, respectively. Si II and Si III have larger differences of 98%, 83%, and 64% from the cool, nominal, and hot models, respectively. The ionization balance of Mg favors the nominal and cooler models, while Fe and Si favor the nominal and hotter models. In GALEXJ2339 total abundances from Mg I and Mg II differ by 50%, 25%, and 30% in the cool, nominal, and hot models, respectively, while the agreement is excellent for Fe I and Fe II at 5%, 1%, and 28%. Both elements have the best accordance with the nominal $T_{\rm eff}$ model. Thus, we find that the ionization balance supports our best-fit (nominal) $T_{\rm eff}$ for each of the two stars.

Table 9
UV-Optical Abundance Comparison for GD 378

Z	FUSE $\log[n(Z)/n(He)]$	HIRES $\log[n(Z)/n(He)]$
O	$-6.12^{+0.20}_{-0.36}$	$-5.94^{+0.19}_{-0.35}$
Si	$-7.43^{+0.14}_{-0.21}$	$-7.58^{+0.04}_{-0.05}$
Fe	$-7.43^{+0.19}_{-0.36}$	$-7.60^{+0.20}_{-0.37}$

ORCID iDs

Beth L. Klein https://orcid.org/0000-0001-5854-675X
Alexandra E. Doyle https://orcid.org/0000-0003-0053-3854
B. Zuckerman https://orcid.org/0000-0001-6809-3045
P. Dufour https://orcid.org/0000-0003-4609-4500
Simon Blouin https://orcid.org/0000-0002-9632-1436
Carl Melis https://orcid.org/0000-0001-9834-7579
Alycia J. Weinberger https://orcid.org/0000-0001-6654-7859
Edward D. Young https://orcid.org/0000-0002-1299-0801

References

Alam, S., Albareti, F. D., Allende Prieto, C., et al. 2015, ApJS, 219, 12
Allègre, C., Manhès, G., & Lewin, E. 2001, E&PSL, 185, 49
Barstow, M. A., Barstow, J. K., Casewell, S. L., Holberg, J. B., & Hubeny, I. 2014, MNRAS, 440, 1607
Barstow, M. A., Boyce, D. D., Welsh, B. Y., et al. 2010, ApJ, 723, 1762
Bergeron, P., Wesemael, F., Dufour, P., et al. 2011, ApJ, 737, 28
Bianchi, L., Shiao, B., & Thilker, D. 2017, ApJS, 230, 24
Blouin, S., Dufour, P., & Allard, N. F. 2018, ApJ, 863, 184
Boesgaard, A. M. 1976a, ApJ, 210, 466
Boesgaard, A. M. 1976b, PASP, 88, 353
Boesgaard, A. M., Armengaud, E., & King, J. R. 2003, ApJ, 582, 410
Boesgaard, A. M., Armengaud, E., King, J. R., Deliyannis, C. P., & Stephens, A. 2004, ApJ, 613, 1202
Boesgaard, A. M., Lum, M. G., & Deliyannis, C. P. 2020, ApJ, 888, 28
Bond, J. C., O'Brien, D. P., & Lauretta, D. S. 2010, ApJ, 715, 1050
Bruhweiler, F. C., & Kondo, Y. 1981, ApJL, 248, L123
Chmielewski, Y., Brault, J. W., & Mueller, E. A. 1975, A&A, 42, 37
Cottrell, P. L., & Greenstein, J. L. 1980, ApJ, 238, 941
Coutu, S., Dufour, P., Bergeron, P., et al. 2019, ApJ, 885, 74
Cummings, J. D., Kalirai, J. S., Tremblay, P.-E., Ramirez-Ruiz, E., & Choi, J. 2018, ApJ, 866, 21
Cutri, R. M., Skrutskie, M. F., van Dyk, S., et al. 2003, yCat, II/246
Dennihy, E., Xu, S., Lai, S., et al. 2020, ApJ, 905, 5
Desharnais, S., Wesemael, F., Chayer, P., Kruk, J. W., & Saffer, R. A. 2008, ApJ, 672, 540
Doyle, A. E., Desch, S. J., & Young, E. D. 2021, ApJL, 907, L35
Doyle, A. E., Klein, B., Schlichting, H. E., & Young, E. D. 2020, ApJ, 901, 10
Doyle, A. E., Young, E. D., Klein, B., Zuckerman, B., & Schlichting, H. E. 2019, Sci, 366, 356
Dufour, P., Bergeron, P., Liebert, J., et al. 2007, ApJ, 663, 1291
Dufour, P., Blouin, S., Coutu, S., et al. 2017, in ASP Conf. Ser., 509, 20th European White Dwarf Workshop, ed. P.-E. Tremblay et al. (San Francisco, CA: ASP), 3
Dufour, P., Kilic, M., Fontaine, G., et al. 2010, ApJ, 719, 803
Dufour, P., Kilic, M., Fontaine, G., et al. 2012, ApJ, 749, 6
Dupree, A. K., & Raymond, J. C. 1982, ApJL, 263, L63
Eisenhardt, P. R. M., Marocco, F., Fowler, J. W., et al. 2020, ApJS, 247, 69
Eisenstein, D. J., Liebert, J., Harris, H. C., et al. 2006, ApJS, 167, 40
Farihi, J. 2016, NewAR, 71, 9
Farihi, J., Brinkworth, C. S., Gänsicke, B. T., et al. 2011, ApJL, 728, L8
Farihi, J., Gänsicke, B. T., & Koester, D. 2013, Sci, 342, 218
Farihi, J., Jura, M., & Zuckerman, B. 2009, ApJ, 694, 805
Flewelling, H. A., Magnier, E. A., Chambers, K. C., et al. 2020, ApJS, 251, 7
Gaia Collaboration, Brown, A. G. A., Vallenari, A., et al. 2018, A&A, 616, A1
Gaia Collaboration, Prusti, T., de Bruijne, J. H. J., et al. 2016, A&A, 595, A1
Gänsicke, B. T., Koester, D., Farihi, J., et al. 2012, MNRAS, 424, 333
Gentile Fusillo, N. P., Gänsicke, B. T., Farihi, J., et al. 2017, MNRAS, 468, 971

Gentile Fusillo, N. P., Manser, C. J., Gänsicke, B. T., et al. 2020, arXiv:2010.13807
Gentile Fusillo, N. P., Tremblay, P.-E., Gänsicke, B. T., et al. 2019, MNRAS, 482, 4570
Giacalone, S., Teitler, S., Königl, A., Krijt, S., & Ciesla, F. J. 2019, ApJ, 882, 33
Girven, J., Brinkworth, C. S., Farihi, J., et al. 2012, ApJ, 749, 154
Greenstein, J. L. 1956, VA, 2, 1299
Greenstein, J. L. 1969, ApJ, 158, 281
Greenstein, J. L. 1976, ApJL, 207, L119
Greenstein, J. L. 1984, ApJ, 276, 602
Hebrard, G., Lemoine, M., Ferlet, R., & Vidal-Madjar, A. 1997, A&A, 324, 1145
Heinonen, R. A., Saumon, D., Daligault, J., et al. 2020, ApJ, 896, 2
Holberg, J. B., Barstow, M. A., Buckley, D. A. H., et al. 1993, ApJ, 416, 806
Holberg, J. B., Barstow, M. A., & Green, E. M. 1997, ApJL, 474, L127
Holberg, J. B., Barstow, M. A., & Sion, E. M. 1998, ApJS, 119, 207
Holberg, J. B., Hubeny, I., Barstow, M. A., et al. 1994, ApJL, 425, L105
Hollands, M. A., Tremblay, P.-E., Gänsicke, B. T., Koester, D., & Gentile-Fusillo, N. P 2021, arXiv:2101.01225
Hoskin, M. J., Toloza, O., Gänsicke, B. T., et al. 2020, MNRAS, 499, 171
Jessberger, E. K., Christoforidis, A., & Kissel, J. 1988, Natur, 332, 691
Jiménez-Esteban, F. M., Torres, S., Rebassa-Mansergas, A., et al. 2018, MNRAS, 480, 4505
Jura, M. 2008, AJ, 135, 1785
Jura, M., Dufour, P., Xu, S., et al. 2015, ApJ, 799, 109
Jura, M., Klein, B., Xu, S., & Young, E. D. 2014, ApJL, 791, L29
Jura, M., Muno, M. P., Farihi, J., & Zuckerman, B. 2009, ApJ, 699, 1473
Jura, M., Xu, S., Klein, B., Koester, D., & Zuckerman, B. 2012, ApJ, 750, 69
Jura, M., & Young, E. D. 2014, AREPS, 42, 45
Kaiser, B. C., Clemens, J. C., Blouin, S., et al. 2021, Sci, 371, 168
Kelson, D. D. 2003, PASP, 115, 688
Kelson, D. D., Illingworth, G. D., van Dokkum, P. G., & Franx, M. 2000, ApJ, 531, 159
Kenyon, S. J., Shipman, H. L., Sion, E. M., & Aannestad, P. A. 1988, ApJL, 328, L65
Kilic, M., Bergeron, P., Kosakowski, A., et al. 2020, ApJ, 898, 84
Klein, B., Blouin, S., Romani, D., et al. 2020, ApJ, 900, 2
Klein, B., Jura, M., Koester, D., & Zuckerman, B. 2011, ApJ, 741, 64
Klein, B., Jura, M., Koester, D., Zuckerman, B., & Melis, C. 2010, ApJ, 709, 950
Koester, D. 1987, in IAU Colloq. 95: Second Conf. on Faint Blue Stars, ed. A. G. D. Philip, D. S. Hayes, & J. W. Liebert (Schenectady, NY: Davis Press), 329
Koester, D. 2009, A&A, 498, 517
Koester, D., Gänsicke, B. T., & Farihi, J. 2014, A&A, 566, A34
Koester, D., & Kepler, S. O. 2015, A&A, 583, A86
Koester, D., Napiwotzki, R., Voss, B., Homeier, D., & Reimers, D. 2005, A&A, 439, 317
Koester, D., Weidemann, V., & Zeidler, E.-M. 1982, A&A, 116, 147
Kuiper, G. P. 1941, PASP, 53, 248
Liebert, J., Wehrse, R., & Green, R. F. 1987, A&A, 175, 173
Lodders, K. 2003, ApJ, 591, 1220
Lodders, K. 2020, arXiv:1912.00844
McMahon, R. G., Banerji, M., Gonzalez, E., et al. 2013, Msngr, 154, 35
Melis, C., & Dufour, P. 2017, ApJ, 834, 1
Melis, C., Farihi, J., Dufour, P., et al. 2011, ApJ, 732, 90
Melis, C., Jura, M., Albert, L., Klein, B., & Zuckerman, B. 2010, ApJ, 722, 1078
Melis, C., Klein, B., Doyle, A. E., et al. 2020, ApJ, 905, 56
Melis, C., Zuckerman, B., Dufour, P., Song, I., & Klein, B. 2018, RNAAS, 2, 64
Moos, H. W., Sembach, K. R., Vidal-Madjar, A., et al. 2002, ApJS, 140, 3
Mullally, F., Kilic, M., Reach, W. T., et al. 2007, ApJS, 171, 206
Raddi, R., Gänsicke, B. T., Koester, D., et al. 2015, MNRAS, 450, 2083
Reddy, B. E., Tomkin, J., Lambert, D. L., & Allende Prieto, C. 2003, MNRAS, 340, 304
Redfield, S., & Linsky, J. L. 2008, ApJ, 673, 283
Rolland, B., Bergeron, P., & Fontaine, G. 2020, ApJ, 889, 87
Rudnick, R. L., & Gao, S. 2003, TrGeo, 3, 1
Schreiber, M. R., Gänsicke, B. T., Toloza, O., Hernandez, M.-S., & Lagos, F. 2019, ApJL, 887, L4
Shipman, H. L., Barnhill, M., Provencal, J., et al. 1995, AJ, 109, 1231
Shu, F. H., Shang, H., Glassgold, A. E., & Lee, T. 1997, Sci, 277, 1475
Sion, E. M., Aannestad, P. A., & Kenyon, S. J. 1988, ApJL, 330, L55
Sion, E. M., Greenstein, J. L., Landstreet, J. D., et al. 1983, ApJ, 269, 253
Sion, E. M., Liebert, J., & Wesemael, F. 1985, ApJ, 292, 477
Swan, A., Farihi, J., Koester, D., et al. 2019, MNRAS, 490, 202
Tody, D. 1986, Proc. SPIE, 627, 733
van Hoof, P. A. M. 2018, Galax, 6, 63
van Maanen, A. 1917, PASP, 29, 258
Vennes, S., Chayer, P., Hurwitz, M., & Bowyer, S. 1996, ApJ, 468, 898
Vennes, S., Kawka, A., & Németh, P. 2011, MNRAS, 413, 2545
Vennes, S., Thejll, P., & Shipman, H. L. 1991, in NATO Advanced Study Institute (ASI) Series C 336, White Dwarfs, ed. G. Vauclair & E. Sion (Dordrecht: Kluwer), 235
Veras, D. 2016, RSOS, 3, 150571
Veras, D., & Heng, K. 2020, MNRAS, 496, 2292
Vogt, S. S., Allen, S. L., Bigelow, B. C., et al. 1994, Proc. SPIE, 2198, 362
Wegner, G. 1981, ApJL, 245, L27
Wehrse, R., & Liebert, J. 1980, A&A, 86, 139
Weidemann, V. 1960, ApJ, 131, 638
Wilson, D. J., Gänsicke, B. T., Koester, D., et al. 2019a, MNRAS, 483, 2941
Wilson, T. G., Farihi, J., Gänsicke, B. T., & Swan, A. 2019b, MNRAS, 487, 133
Xu, S., Dufour, P., Klein, B., et al. 2019, AJ, 158, 242
Xu, S., Jura, M., Klein, B., Koester, D., & Zuckerman, B. 2013, ApJ, 766, 132
Xu, S., Zuckerman, B., Dufour, P., et al. 2017, ApJL, 836, L7
Zuckerman, B. 2015, in ASP Conf. Series 493, 19th European Workshop on White Dwarfs, ed. P. Dufour et al. (San Francisco, CA: ASP), 291
Zuckerman, B., Koester, D., Dufour, P., et al. 2011, ApJ, 739, 101
Zuckerman, B., Koester, D., Melis, C., Hansen, B. M., & Jura, M. 2007, ApJ, 671, 872
Zuckerman, B., & Young, E. D. 2018, Handbook of Exoplanets (Cham: Springer International), 1545